Journal of Structural Geology 33 (2011) 169–186

Contents lists available at ScienceDirect

Journal of Structural Geology

journal homepage: www.elsevier.com/locate/jsg

Pseudotachylyte in muscovite-bearing quartzite: Coseismic friction-induced melting and plastic deformation of quartz

Michel Bestmann [a,*], Giorgio Pennacchioni [b,c], Gerhard Frank [d], Mathias Göken [e], Helga de Wall [a]

[a] GeoZentrum Nordbayern, University of Erlangen-Nuremberg, Germany
[b] Department of Geosciences, University of Padova, Italy
[c] Istituto Nazionale di Geofisica e Vulcanologia, Roma, Italy
[d] Department Werkstoffwissenschaften VII, University of Erlangen-Nuremberg, Germany
[e] Department Werkstoffwissenschaften I, University of Erlangen-Nuremberg, Germany

ARTICLE INFO

Article history:
Received 12 January 2010
Received in revised form
16 September 2010
Accepted 30 October 2010
Available online 5 November 2010

Keywords:
Pseudotachylyte
Quartz
Microstructures
Plastic deformation
EBSD
TEM

ABSTRACT

Thin (0.5–2 mm thick) pseudotachylyte veins occur within muscovite-bearing (~10% volume), amphibolite-facies quartzites of the Schneeberg Normal Fault Zone (Austroalpine, Southern Tyrol, Italy). Pseudotachylytes are associated with precursor localized plastic microshear zones (50–150 μm thick) developed sub-parallel to the host-rock foliation and with conjugate sets oriented at a high angle to the foliation. Such microshear zones are characterized by recrystallization to ultrafine-grained (1–2 μm grain size) mosaic aggregates of quartz showing a transition from a host-controlled to a random crystallographic preferred orientation towards the shear zone interior. Subsequent coseismic slip mainly exploited these microshear zones. Microstructural analysis provides evidence of extensive friction-induced melting of the muscovite-bearing quartzite, producing a bimodal melt composition. First, the host-rock muscovite was completely melted and subsequently crystallized, mainly as K-feldspar. Then, about 60% volume of the ultrafine-grained quartz underwent melting and crystallized as spherulitic rims (mostly consisting of quartz ± Ti ± Fe) around melt-corroded quartz clasts. The two melts show immiscibility structures in the major injection veins exploiting microshear zones at high angles to the quartzite foliation. In contrast, they were mechanically mixed during flow along the main fault veins.

1. Introduction

Tectonic pseudotachylytes are solidified friction-induced melts produced along a fault during seismic slip (i.e. at slip rates of 1–3 ms^{-1}) (Sibson, 1986; Spray, 1992; Swanson, 1992; Sibson and Toy, 2006; Lin, 2008; Di Toro et al., 2009 and references within). They have been reported in a large variety of silicate-built rocks including felsic to mafic-ultramafic intrusive rocks and different metamorphic rocks (Sibson and Toy, 2006; Di Toro et al., 2009). However, pseudotachylytes within quartzites have not been reported previously.

Non-equilibrium melting is inferred to be the dominant process during friction-induced melting as indicated by the disappearance, or a decrease in the percentage, of host-rock clasts of low-melting point minerals (e.g. micas and amphiboles) in the pseudotachylyte. Preferential melting of mafic minerals (having relatively low single-phase melting point) results in a more basic composition of the pseudotachylyte melt (or matrix) than the host-rock, whereas the bulk pseudotachylyte composition (clasts + matrix) is identical to that of the host-rock (Allen, 1979; Bossière, 1991; Camacho et al., 1995; Maddock, 1986, 1992; Magloughlin, 1989; Sibson, 1975; Spray, 1992, 1993; Di Toro and Pennacchioni, 2004). In pseudotachylytes from within granitoid rocks: (i) biotite melts completely, (ii) plagioclase (with a melting temperature under dry conditions in the range of 1100–1550 °C) undergoes partial to complete melting in the centre of centimetre thick veins, indicative of superheating of friction-induced melts (Di Toro and Pennacchioni, 2004), and (iii) quartz, having a very high melting temperature (1720 °C under dry conditions; Deer et al., 1992), commonly survives as clast, although embayed shapes have been reported as local evidence of quartz melting (Lin, 2008 and references within). In addition to the high melting point of quartz, the friction-induced melting of this mineral is potentially hindered by the occurrence of extreme fault weakening at high slip rates; this has been experimentally determined in quartzite and related to lubrication by silica gel (Di Toro et al., 2004).

* Corresponding author.
E-mail address: michel@geol.uni-erlangen.de (M. Bestmann).

0191-8141/$ – see front matter © 2010 Elsevier Ltd. All rights reserved.
doi:10.1016/j.jsg.2010.10.009

The maximum temperature achieved during friction-induced melting is an important parameter for estimating the energy budget of an earthquake from exhumed paleoseismic faults (Di Toro et al., 2005). To estimate this temperature, minerals surviving melting have often been used (e.g. Maddock, 1983). The commonly reported range of estimated and inferred friction melt temperatures is 650–1730 °C (Sibson and Toy, 2006). The observation of quartz melting could therefore provide evidence for unusually high thermal peaks (in a dry environment). The amount of quartz involved in melting to form a pseudotachylyte cannot be easily quantified. Spherulitic overgrowth structures around quartz clasts have been described in some pseudotachylytes (e.g. "quartz-nucleus spherulites": Lin, 1994; Di Toro and Pennacchioni, 2004), where inclusion-rich quartz rims surround rounded quartz clasts. However, these features cannot be univocally related to the achievement of single-quartz melting point.

In this study, we report on the occurrence of pseudotachylytes within muscovite-bearing (~10% volume) amphibolite-facies quartzites of the "Schneeberg Normal Fault Zone" (Austroalpine, Southern Tyrol, Italy) clear evidence of extensive frictional melting of quartz. The detailed microstructural and electron microscope analysis (scanning electron microscopy – SEM, electron backscatter diffraction technique – EBSD, and transmission electron microscopy – TEM) show a close spatial association between pseudotachylytes and ultrafine-grained aggregates (grain size in the order of a few microns) delineating microshear zones in the host quartzite close to the fault vein.

2. Methods

2.1. Sample preparation

Optical microscopy (transmitted light) and SEM analysis were carried out on oriented samples. Polished thin-sections were obtained from slabs cut parallel to the mineral lineation (X-axis) and perpendicular to the foliation (XY plane) of the quartzite hosting the pseudotachylyte. The XZ section is also orthogonal to the pseudotachylyte veins. EBSD measurements (Section 5.1.2) have shown that this reference frame also contains the main kinematic axes of the network of microshear zone precursors of seismic slip. For SEM analyses, the thin-sections were chemical polished using a colloidal silica suspension (SYTON) and subsequently carbon coated (coating thickness of ca. 3 nm).

2.2. SEM analysis

SEM analyses were carried out with a ZEISS *CrossBeam* 1540 EsB equipped with a thermo-ionic field emission located at the Department of Material Sciences of the University Erlangen-Nuremberg. The cathodoluminescence (CL) images of Fig. 10d was produced with a TESCAN Vega-XM-U SEM attached with a CL-system.

2.3. EBSD

Full crystallographic orientation data were obtained from automatically indexed EBSD patterns collected in beam scan mode on a 0.2 and 0.3 μm grid (working conditions: working distance 16 mm, 20 kV acceleration voltage, 120 μm aperture and high current mode resulting in ca. 7 nA beam current). The stored EBSD patterns were indexed by using the program CHANNEL 5.09 from Oxford Instruments. The centre of 8 Kikuchi bands was automatically detected using the Hough transform routine (Schmidt et al., 1991; Adams et al., 1993) with a resolution of 120 (internal Hough resolution parameter in the software). The solid angles calculated from the patterns were compared with the mineral specific match unit (muscovite, quartz and/or orthoclase) containing 75 reflectors to index the patterns.

EBSD orientation data are presented as processed orientation maps. Non-indexed points were replaced by the most common neighbouring orientation. The degree of processing required to fill non-indexed data points, without introducing artefacts, was tested carefully by comparing the resulting orientation map with the pattern quality map (Bestmann and Prior, 2003).

2.4. TEM

The TEM foils were examined at 300 kV in a Phillips CM 30 Twin/STEM transmission electron microscope at the Central Facility for High Resolution Electron Microscopy of the University Erlangen-Nuremberg. All diffraction contrast images were produced using bright field (BF) conditions. Geochemical energy-dispersive spectroscopy (EDS) analyses (element mapping and line scans) were carried out in the scanning transmission electron microscopy (STEM) mode with an Oxford Instrument ISIS 300 EDS system, using a Si(Li) detector.

Two different sample preparation methods were applied for the TEM analysis. Samples of 1 inch size were assembled with a 200 μm spaced copper net for conventional ion beam thinning with a BAL-TEC BALZER RES 010 (thinning parameter: inclination angle 11–12°, acceleration voltage 3.5–5 kV). This sample preparation was not appropriate for geochemical area analyses in the TEM because in a polyphase rock, such as the pseudotachylyte, a sample topography could not be excluded. Such small-scale irregularities on the sample surface might cause thickness-dependent artefacts especially in EDS line scans and element mappings. To guarantee plane parallel electron-transparent foils, the focussed ion beam (FIB) technique was applied. This technique allows site specific TEM foils (10–20 μm wide, 5–15 μm high and 100–200 nm thick) to be prepared through Ga-ion beam thinning on standard thin-sections. The TEM foils were prepared using a ZEISS *CrossBeam* 1540 EsB at the Material Science Department at the University Erlangen-Nuremberg.

2.5. Electron microprobe analysis (EMPA)

Compositional data of muscovite and K-feldspar were measured on a Jeol JXA-8200 at the GeoZentrum Nordbayern (University of Erlangen-Nuremberg). Natural silicates were used as standards and a ZAF routine was applied for matrix correction. Measuring conditions using a focussed electron beam were: 15 kV acceleration voltage and 15 nA beam current.

2.6. Image analysis

Image analysis was performed on the quartzite and pseudotachylyte veins in order to estimate the relative amounts of minerals and of the different fabric elements within the pseudotachylyte (i.e. matrix, quartz clasts and spherulitic quartz overgrowth on clasts). Image analysis was carried out with DIAna software (©J. Duyster).

Host-rock volume percentage of quartz, muscovite and K-feldspar were determined from manual drawings from light optical microscope images. The analysis of pseudotachylyte veins was performed automatically on SEM-BSE images using a greyscale range selection option in the DIAna software.

3. Geological setting

The Schneeberg Normal Fault Zone (SNFZ) is developed in the Schneeberg/Monteneve Unit (SMU) which belongs to the composite Austroalpine nappe of the central-Eastern Alps that was

derived from the Jurassic paleo-Adriatic continental margin. The SNFZ outcrops NW of Meran/Merano, in a tectonically complex area located W of the Southalpine indenter, close to a major bend of the Periadriatic lineament (Fig. 1a). In this region, the Austroalpine domain consists of a stack of N – NW-dipping tectonic units namely, from top to bottom: (a) Ötztal-Stubai, (b) Schneeberg-Monteneve, (c) Texel and (d) Campo-Ortler/Mauls-Penserjoch (Fig. 1b, c). Units (a) and (d) consist of basement rocks (mainly paraneisses and orthogneisses) preserving a dominant amphibolite, partly eclogite-facies Carboniferous (375–310 Ma) metamorphic imprint. Unit (d) also contains Permian intrusives. Units (b) and (c) show a dominant amphibolite- to eclogite-facies Cretaceous metamorphic imprint from ca. 95–80 Ma ago (Sölva et al., 2005; Habler et al., 2006; Hoinkes and Thöni, 1987) that in (c) overprint pre-Cretaceous amphibolite-facies assemblages. Note that the SMU, which consists of garnet micaschists, marble layers, amphibolites, quartzites, hornblende-garbenschiefer and calcsilicate schists, does not show relicts of pre-Cretaceous metamorphism. These rocks underwent a polyphase deformation history, representing an about 4.5 km thick extensional shear zone (Schneeberg Fault Zone, Sölva et al., 2005). Exhumation started around 95 Ma from high-P amphibolite-facies (ca. 1.0 GPa and 600 °C at 95 Ma, constrained from garnet Sm–Nd data, Konzett and Hoinkes, 1996; Sölva et al., 2005) and persisted to low greenschist-facies/brittle conditions at 76 Ma (constrained from biotite Rb–Sr data, Sölva et al., 2005), with a consistent top-to-(W) NW kinematics and a progressive localization of strain during decreasing temperature. Pseudotachylytes were described as developing along late-stage brittle faults. The Schneeberg Fault Zone was interpreted to represent the hanging wall normal fault of an extruding wedge (represented by the Texel Complex), in which Cretaceous eclogite-facies metamorphic rocks were exhumed (Sölva et al., 2005).

4. Outcrop and samples description

The study samples were collected from a quartzite layer, of about 10 m thickness, within garnet micaschists of the SMU (Fossental; GPS: E653553/N5180119, Zone 32N UTM WGS 84). Both in the field and hand samples, the quartzite shows a colour banding (Fig. 2), that does not correspond to any obvious mineral variation in thin-sections, and defines a foliation. The quartzite contains thin (less than 2 mm thick), sharply-bounded dark pseudotachylyte veins mainly forming fault veins (*sensu* Sibson, 1975) oriented subparallel or at a low angle to the quartzite foliation and with no connection to the flanking micaschists. In detail, these layer-parallel pseudotachylyte veins have local variations in thickness and show breccia-like structures at contractional bridges connecting adjacent, overlapping en-echelon slip surfaces spaced a few centimetres apart and forming paired shears in the overlapping zone. The studied samples include one such contractional domain, formed between two main slip surfaces, referred to as fault$_{1a}$ and *fault*$_{1b}$ (Fig. 2b). The main faults$_1$ are connected by linkage veins (e.g. *fault*$_2$) in the contractional domain. In proximity to the pseudotachylyte vein forming the "relay ramp" linking *fault*$_{1a}$ and *fault*$_{1b}$, and within the contractional bridge, the foliation is distorted and folded. The fold asymmetry on the ramp structure is consistent with the normal sense of shear along the main faults. Small (a few millimetres long) injection veins intrude the host quartzite, branching off at a high angle to *fault*$_{1a}$.

Conjugated sets of extensional *faults*$_3$, decorated by pseudotachylyte veins, extend at a high angle from *fault*$_{1a}$ into the host quartzite. The offset of the main foliation across major *faults*$_3$ is on the order of 5 mm and can be seen in hand samples (Fig. 2b). In addition to major *faults*$_3$, the host quartzite contains numerous smaller incipient *faults*$_3$, with offsets in the order of a few millimetres or less, forming a lozenge shaped pattern overprinting the foliation (Fig. 5f). The pseudotachylyte veins along the *fault*$_{1a}$ show thickening at their intersection with *fault*$_3$ but are not offset by these structures.

5. Microstructures

5.1. Host-rock quartzite

5.1.1. Undamaged host-rock

The host-rock quartzites contain muscovite (10–12% in volume), in oriented isolated flakes defining the foliation, and K-feldspar (1–2%). The K-feldspar occurs as small isolated grains or as a local partial replacement of muscovite. Muscovite contains 2–7 wt % FeO, up to 2.6 wt % TiO_2 and up to 2 wt % MgO. It is associated with an Fe-phase, mainly hematite (~1 vol.%). Accessory minerals are biotite, rutile, ilmenite, apatite and zircon.

The quartzite away from the pseudotachylytes consists of large grains, up to 500 μm in size, preferentially elongated parallel to the foliation (Fig. 3). Quartz grains have irregular lobate boundaries and quartz–quartz boundaries tend to form a 90° angle with the muscovite {001} plane. These microstructures are typical of high grade metamorphic conditions and grain boundary migration recrystallization consistent with the peak metamorphism of the SMU unit.

5.1.2. Fault-related deformation microstructures in the quartzite

Close to and/or between pseudotachylyte veins, and where the quartzite host foliation is folded towards the main pseudotachylyte-bearing fault, the quartzite shows deformation microstructures (Figs. 2b, 5 and 6) that are absent in the host-rock away from the fault (Fig. 3). These microstructures include: (i) pervasive fine

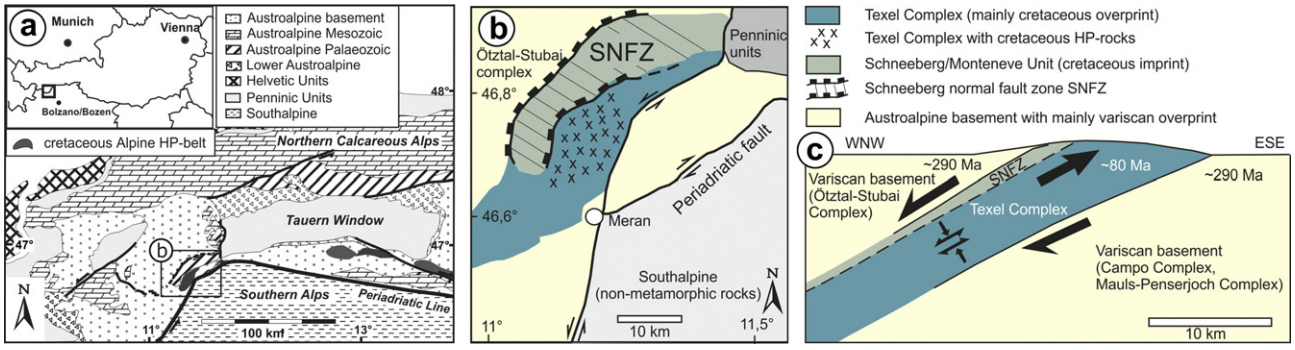

Fig. 1. (a) Tectonic map of the Eastern Alps (modified after Frey et al., 1999); (b) map of the tectonic units around the Schneeberg/Monteneve Unit and Texel Complex (after Sölva et al., 2005); (c) schematic model of Cretaceous Alpine E–SE-directed exhumation of HP rocks within an extruding wedge (after Sölva et al., 2005). The Schneeberg Normal Fault Zone (SNFZ) represents the upper thrusting boundary of the wedge. Age data at ~80 Ma indicate cooling below 300 °C after (Sölva et al., 2005).

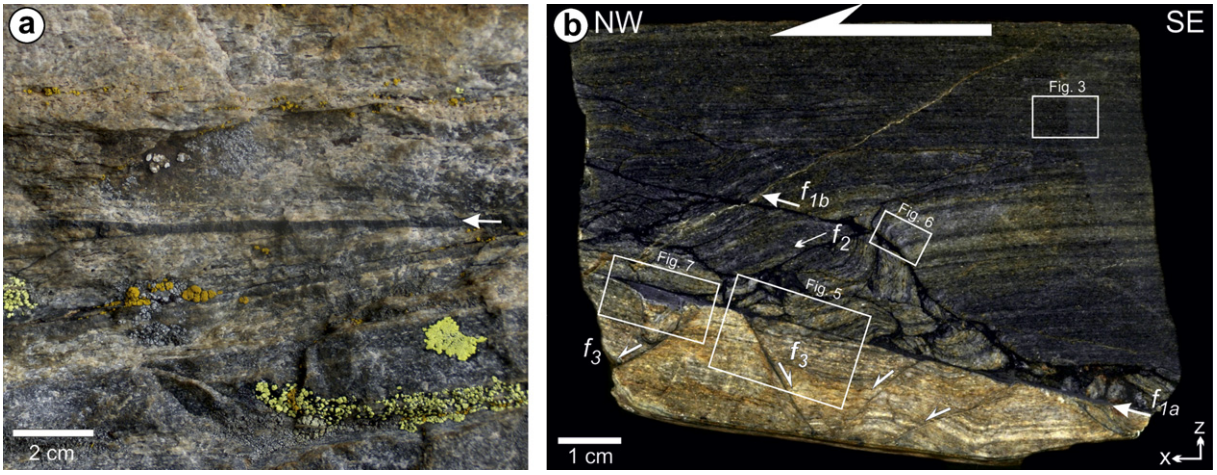

Fig. 2. (a) Pseudotachylyte fault vein (indicated by the white arrow) sub-parallel to the main foliation of the host muscovite-bearing quartzite. (b) Polished sample of the study pseudotachylyte. Pseudotachylyte occurs in different types of veins: *fault*$_{1a}$ and *fault*$_{1b}$ veins are sub-parallel to the main foliation in the quartzite; *faults*$_2$ are linkage veins connecting *fault*$_{1a}$ and *fault*$_{1b}$ en-echelon segments in the contractional bridge; and *fault*$_3$ veins are conjugate sets at a high angle to the foliation. The sense of shear along the main fault zone is sinistral. The colour variation across the main fault vein does not correspond to any detectable compositional variation of the quartzite.

kinking of muscovite (Fig. 4b–e), and (ii) patchy undulatory extinction, deformation bands, deformation lamellae and small new grains (grain size < 2 μm) along inter- and intragranular microshear zones in quartz (Figs. 5–7).

The muscovite deformation microstructure is similar to that reported in muscovite-rich cataclasites associated with pseudotachylytes in the Siberia Fault Zone (White, 2001) and, for biotite, in the damaged tonalite flanking pseudotachylyte-bearing faults in the Adamello (Di Toro and Pennacchioni, 2005). EBSD analysis reveals lattice bending and kinking of {001} planes and the development of subgrain boundaries due to rotation around crystallographic axes (<−310> and/or <010>) that are sub-parallel to the bulk vorticity axis Y (Fig. 4e) (see also Bell et al., 1986).

Ultrafine-grained microshear zones occur adjacent, and sub-parallel or at a low angle, to the pseudotachylytes veins within the quartzite (Fig. 5). These inter- and intragranular microshear zones, are delineated by aggregates of ultrafine-grained (0.5–2.5 μm) quartz (Fig. 8h). An offset (100–200 μm) is sometimes evident on intragranular shear zones (Fig. 5bII, f and in supplementary online material, Fig. SOM1). The intergranular microshear zones occur as 50–150 μm thick discontinuous layers, especially along contacts between the host quartzite and the *fault*$_{1-3}$ pseudotachylytes (Fig. 5c). The microstructure and crystallographic preferred orientation (CPO) of quartz in the microshear zones was investigated by combined optical microscopy, SEM-OC, EBSD and TEM. Representative EBSD-datasets are shown in Fig. 9 and in Fig. SOM1-4 (supplementary online material). The orientation contrast images (Fig. 8a, b) and EBSD orientation map (Fig. 9a) reveal that the host quartz grains contain localized deformation zones with a high subgrain boundary density.

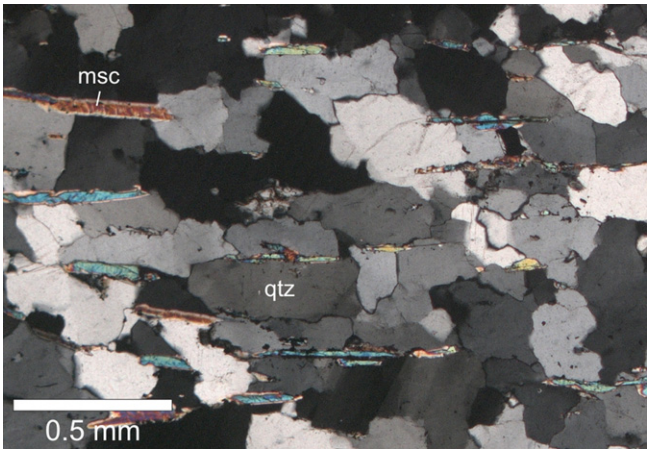

Fig. 3. Optical micrograph (crossed polars) of the amphibolite-facies host-rock showing the "undamaged" coarse-grained quartzite (qtz) including isolated aligned lamellae of muscovite (msc) outlining the foliation.

Towards the microshear zone, the size of subgrains decreases and the orientation contrast pattern becomes diffuse. Related to these highly deformed host domains, TEM images show both the local appearance of a high dislocation density and the preferential arrangement of dislocations to define a subgrain mosaic (main subgrain size of 300–500 nm) (Fig. 8e). The "subgrain" walls consist either of disordered dislocations or of ordered arrays dislocations. Towards the interior of microshear zones, the subgrain microstructure merges into an aggregate of individual ultrafine grains (Fig. 8c, d and f) that are also evident in the orientation map (Fig. 9) (i.e. individual grains are entirely surrounded by high angle boundaries with a misorientation angle $> 15°$, see Bestmann and Prior, 2003). These new grains have straight or slightly curved boundaries and build a mosaic of polygonal grains with triple grain junctions at 120°, and grain sizes in the range of 0.5–2 μm, i.e. slightly larger than subgrains (Fig. 8c, d, f, g and h). They are in general free of dislocations (Fig. 8g). The new grain boundaries are locally decorated with regular arrays of fluid inclusions (Fig. 8d and g) similar to grain boundary pores commonly described in quartz mylonites (e.g. Mancktelow and Pennacchioni, 2004).

Both the orientation maps and the crystallographic orientation plots reveal a gradual lattice bending of the host quartz towards the highly-distorted area which merges into the microstructure with new small grains (Fig. 9a). The pole figures show a rotation of the lattice around one crystallographic *a*-axis (up to 45° in the highly-distorted areas) in a synthetic sense when compared with the sense of shear in the associated microshear zone. For all analysed microstructures (see also Fig. SOM1–3), the lattice deflection generally occurs around an axis (sub)parallel to the Y-axis, i.e. coinciding with the vorticity axis of the bulk fault zone (see also Section 2.1; Bestmann and Prior, 2003).

The CPO of the small new grains, adjacent to the highly-distorted area, scatters statistically around the orientation of the

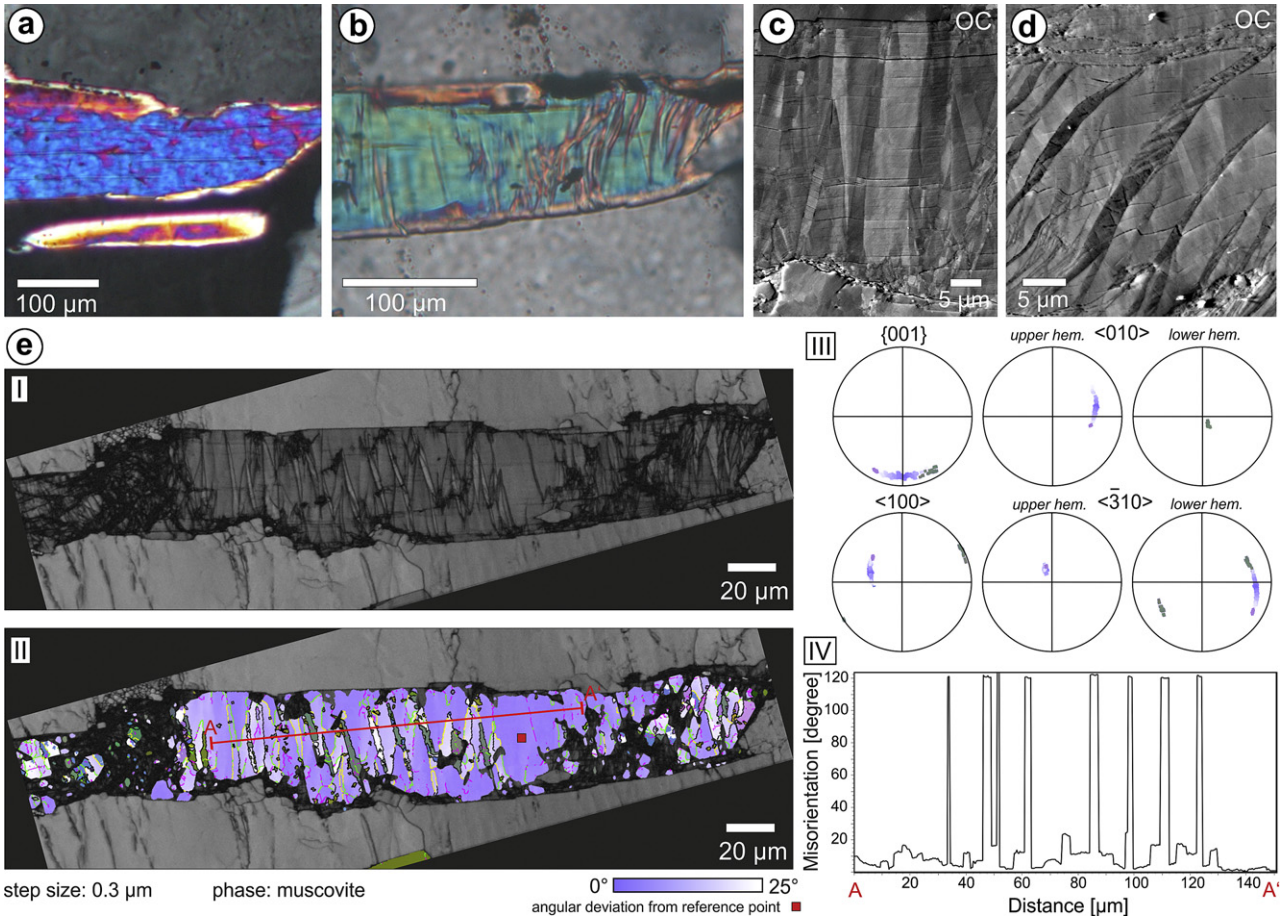

Fig. 4. Micrograph (crossed polars) of (a) undeformed and (b) deformed muscovite. (c, d) SEM-OC (orientation contrast due to electron channelling processes) image of micro-kinks and subgrain mosaic within deformed muscovite. (e) EBSD data of deformed muscovite. [I] Patten quality (band contrast) map. [II] Orientation map. Each pixel represents an orientation, colour coded with respect to its Euler angles. Substructure is colour coded according to angular deviation from a given reference point (red square). Grey pixels are quartz or non-index points of muscovite. Purple, yellow and green lines mark subgrain boundaries (misorientation <15°), black lines indicate high angle boundaries (>15°). [III] Orientation data along misorientation line (red) are presented as pole figures (equal area upper hemisphere stereoplots of main {planes} and <axes> of muscovite). Note lattice deflection around <−310> and/or <010>. [IV] Misorientation profile A–A'; the continuous change of misorientation angle is displayed with respect to the first point A.

distorted host grain (area-2 in Fig. 9a and Fig. SOM1-3). In contrast, the small grains from the interior of the microshear zones show a nearly random CPO with a very weak maximum inherited from the host quartz (area-3 in Fig. 9a). This random CPO is also evident for the intergranular microshear zones that typically form discontinuous layers (50–150 µm in thickness) at the contact between the quartzite host-rock and the *fault*$_{1-3}$ pseudotachylytes veins (Fig. 9b). Coarser remnants of the host-rock material within these ultrafine-grained intergranular microshear zones may show a high dislocation density and subgrain structure. All the quartz deformation microstructures described in the host-rock also occur in clasts embedded within the pseudotachylyte matrix (Figs. 8i, j and 9b).

5.2. Pseudotachylyte

Pseudotachylytes consist of a matrix derived from solidification and crystallization of a frictional melt (see Section 6.2). Glass and devitrification microstructures have not been observed. Quartz clasts within the pseudotachylyte matrix were derived from both the coarse quartzite grains and the ultrafine-grained recrystallized aggregates (see Section 6.3). The quartz clasts show different microstructures and have been differently modified during the high temperature stages related to melting (see Section 6.3).

5.2.1. Quartz clasts and quartz overgrowths (spherulites) in pseudotachylyte

Quartz clasts (*qtz-1*) range in size from <1 µm to a few 100 µm (Figs. 7a, 8i, 10 and 12a, b) with a dominant grain size of 0.5–3 µm, similar to the grain size of quartz aggregates within the microshear zones of the host quartzite (Fig. 11b). They have a variable shape, from angular to rounded, depending on their position within the pseudotachylyte veins. Some coarse (10's to 100's µm in size) clasts show embayments (Fig. 13a). Coarse clasts are both single crystals and polycrystalline, the latter consisting of fragments of the ultrafine-grained microshear zones (Figs. 8i and 9b) typically developed in the quartzite adjacent to the pseudotachylytes. Similar to the description of the microshear zones in the host quartzite, the polycrystalline clasts consists of a compact, ultrafine-grained microstructure with a nearly random CPO (Fig. 9b-II).

Cathodoluminescence (CL) shows bright, thin (<1 µm) rims around quartz clasts (Fig. 10d). Locally, within polycrystalline quartz aggregates, a bright diffuse CL pattern may appear related to an ultrafine-grained microstructure. In SEM-BSE (back-scattered electron) images such clasts show a transition from a discontinuous decoration of the quartz grain boundaries of the ultrafine-grained microstructure from tiny blebs of K-feldspar ± muscovite (inner part of the clast) to a honeycomb microstructure (outer part), where the single small quartz grains are completely

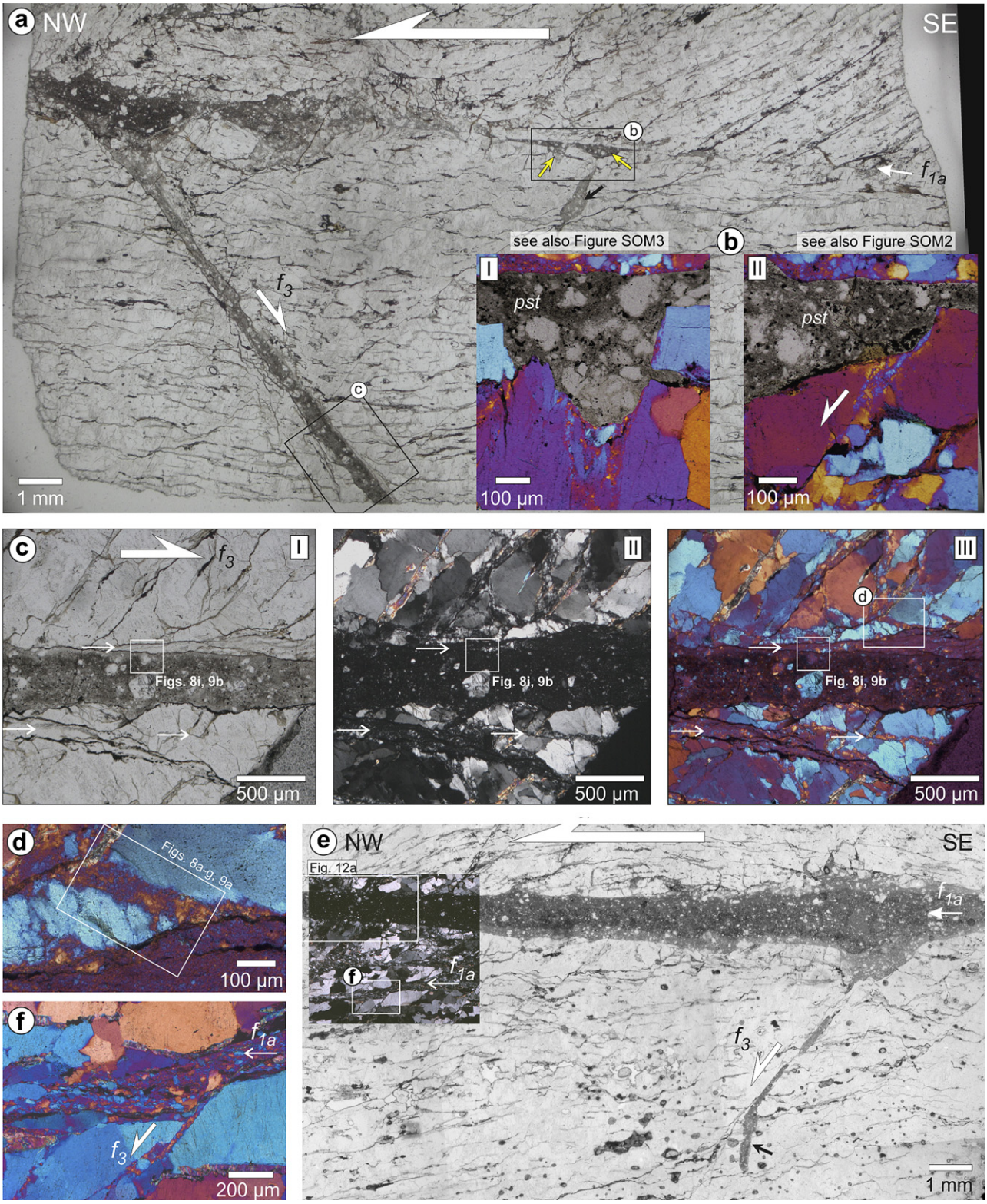

Fig. 5. Optical microstructures of the pseudotachylyte-bearing fault network. (a) Thin-section view (plane parallel light) of *fault*$_{1a}$ and one major antithetic *fault*$_3$. The orientation of the main foliation in the quartzite ranges from sub-parallel to *fault*$_{1a}$ (lower part) to oblique (upper part), inclined to up 30° and abutting abruptly against the slip surface. Some small pseudotachylyte pockets (yellow arrow) and injection vein (black arrow) are marked along *fault*$_{1a}$. (b) Enlargements in [I] and [II] (photomontage of plane parallel light - pseudotachylyte, *pst* - and crossed polars with additional gypsum plate - quartz, *qtz*) show that fault vein pockets are controlled by the intersection of localized microshear zones, at high angle to the slip surface, with *fault*$_{1a}$ (see also Figures SOM2 and 3). Note in [I] the offset of clast along microshear zone. (c) Detail of *fault*$_3$ (f_3) (I: plane polarized light; II: crossed polars; III: crossed polars and gypsum plate). White arrows indicate localized ultrafine-grained microshear zones in the "damaged" quartzite host adjacent and (sub)parallel to the pseudotachylyte vein. Note dextral sense of shear is given because of antithetic *fault*$_3$ set. (d) Intragranular microshear zone within a deformed host quartz (location is shown in c-III); see Fig. 8a–g for detailed SEM and TEM microstructures. (e) Thin-section view (plane parallel light) of *fault*$_{1a}$ and one major synthetic *fault*$_3$ extending on the right side of (a), showing the location of (f) and of images in Fig. 12a. (f) Two microshear zones within quartzitic host-rock at few millimetres distance from the main *fault*$_{1a}$ oriented both parallel to the *fault*$_{1a}$ (f_{1a}) vein and to synthetic *fault*$_3$ veins.

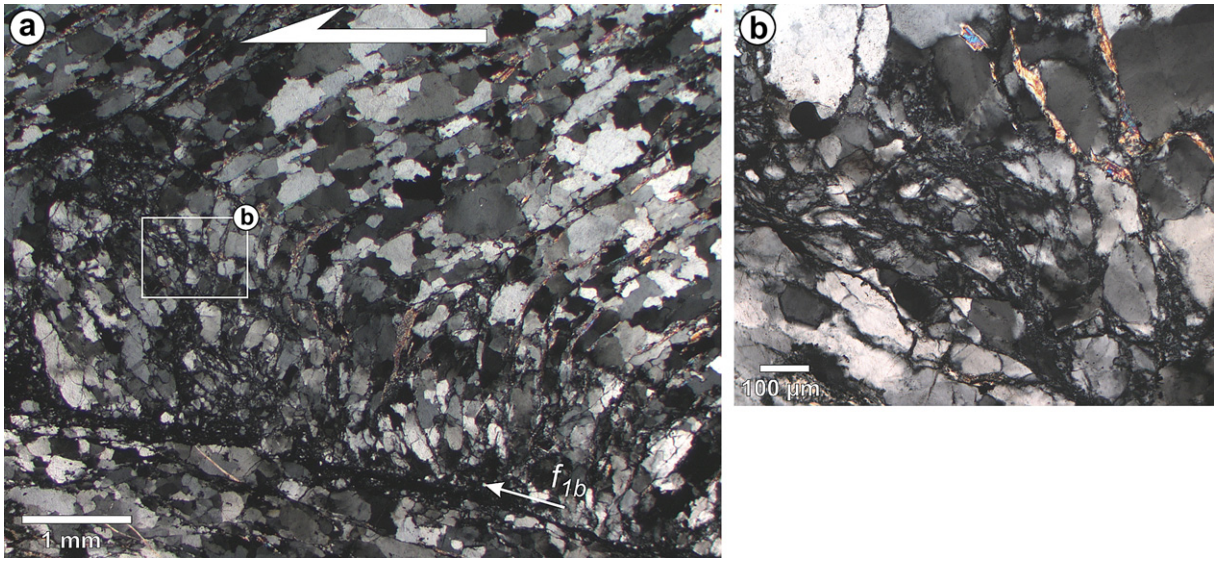

Fig. 6. (a) Distorted and folded quartz host foliation towards the main pseudotachylyte-bearing fault plane. (b) Enlargement of deformation microstructure.

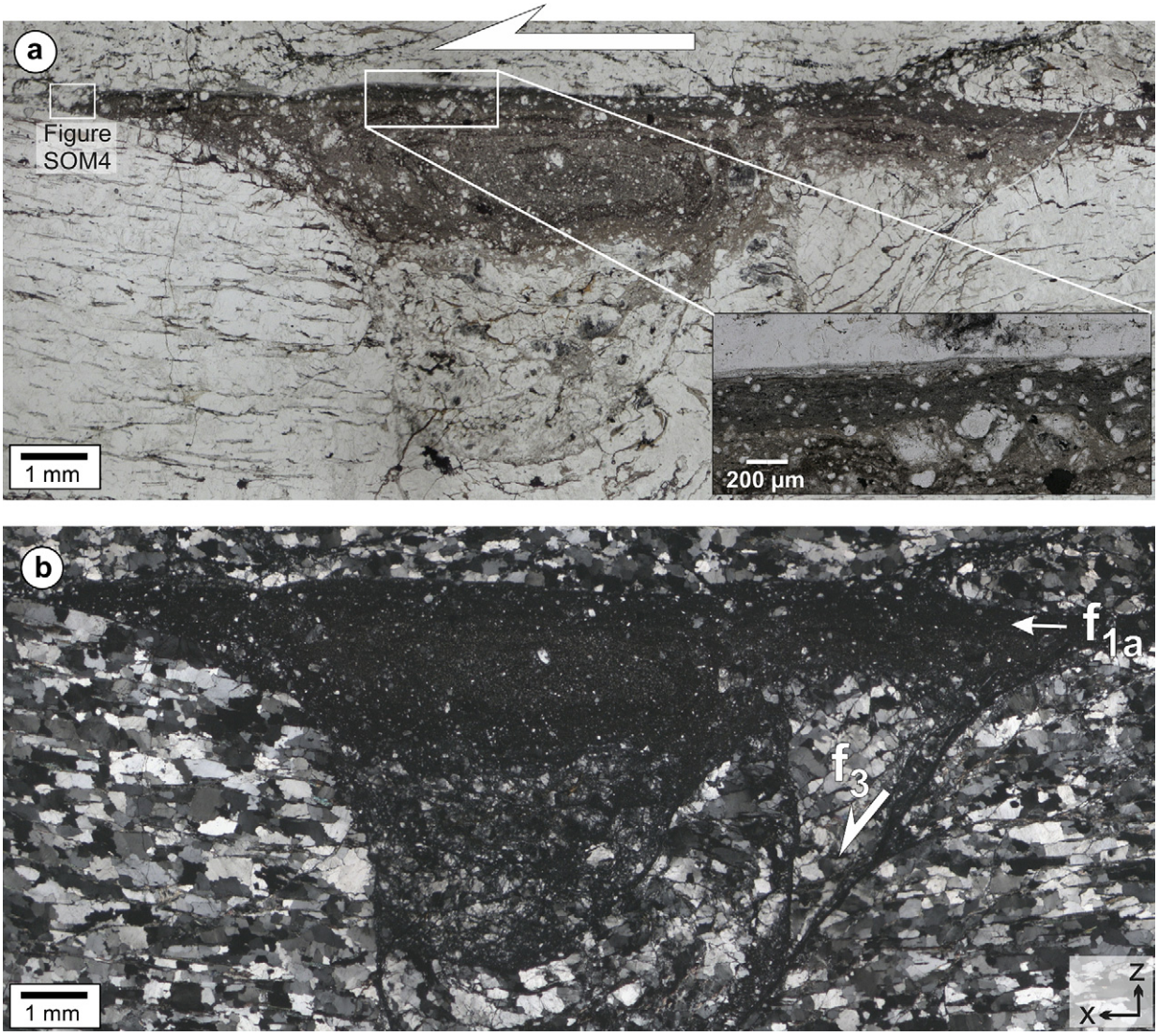

Fig. 7. Eye-shaped flow structure (likely a section of a sheath fold) within the main *fault*$_{1a}$ vein. Micrographs with (a) plane polarized light and (b) crossed polarized light. The flow streaks are marked by colour banding in (a). Note crushed host-rock below eye-shaped fault vein pocket.

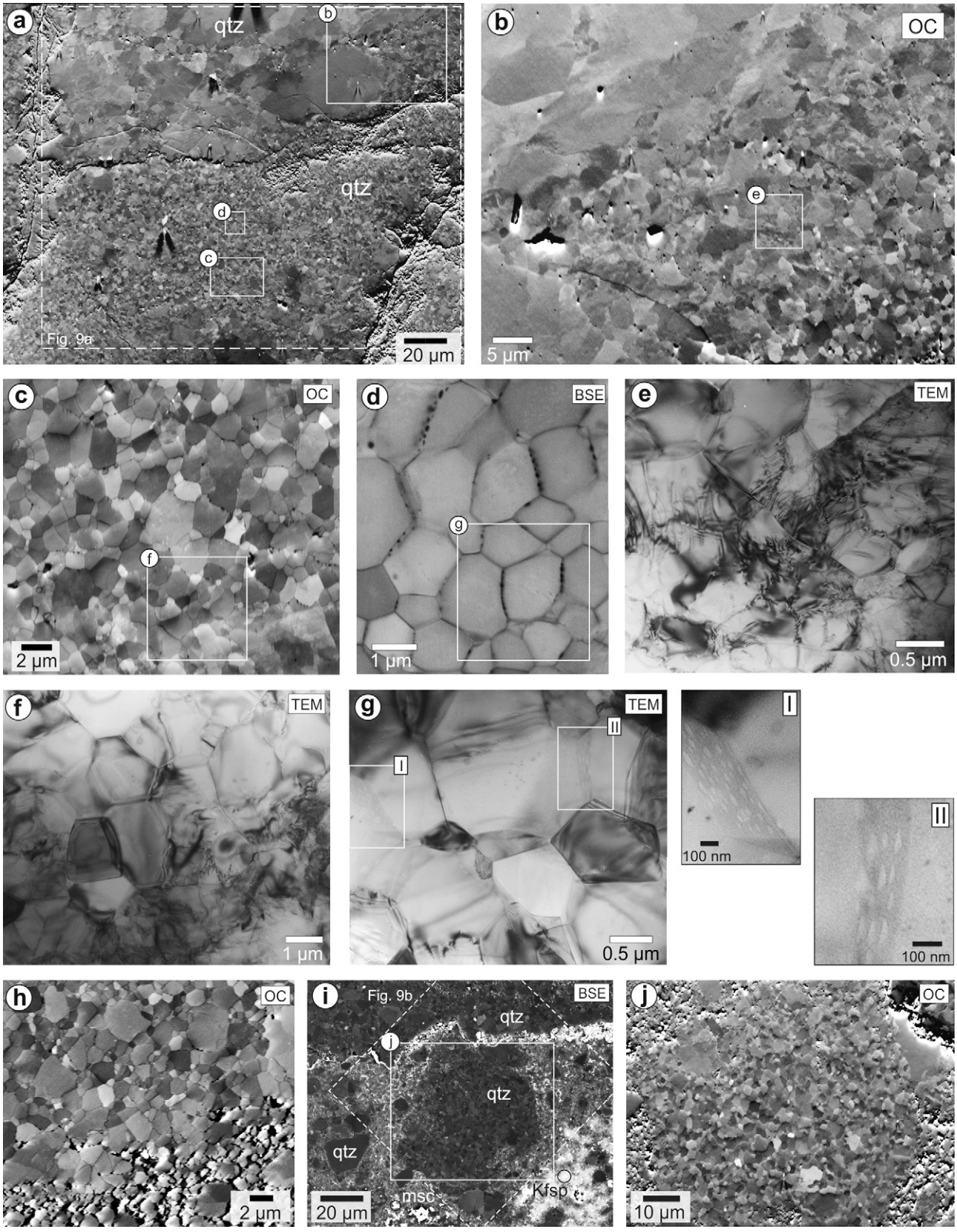

Fig. 8. (a–g) Intragranular microshear zone within quartzitic host-rock, marked in Fig. 5d. (a) SEM-OC image showing the coarsely polygonized host quartz grain in the upper part and an ultrafine aggregate in the lower part and upper right corner. The white rectangles show the areas investigated in detail. The same area (dashed rectangle) was analysed by EBSD (see Fig. 9a). (b) SEM-OC image of the transition zone from the deformed host quartz grain and the ultrafine-grained quartz aggregates typical of the microshear zone. (c) SEM-OC image of the microshear zone interior showing the ultrafine-grained microstructure. (d) High magnification BSE image of the microshear zone interior showing a polygonal microstructure with grain boundaries decorated by fluid inclusions (black dots). (e–g) TEM (BF) images of across the intragranular microshear zone: (e) subgrain polygonization

surrounded by the K-feldspar ± muscovite matrix (Fig. 10b and c). This process of progressive invasion along the former grain boundary structure leads to disaggregation of the ultrafine-grained quartz aggregates into small quartz clasts (grain size of 0.5–3 μm) (Fig. 10c).

Initial pseudotachylyte microstructures preserved along the main fault planes (*fault1$_a$*) show that the ultrafine-grained portion of quartz clasts within the pseudotachylyte matrix is in part predetermined by the grain size refinement of quartz along the microshear zones which preceded seismic faulting (Fig. 11b). In fact, the large dominance of quartz clasts with a small grain size of 0.5–2 μm within the pseudotachylyte veins mostly results from cataclastic disaggregation by grain boundary parting of the ultrafine-grained recrystallized quartz, initially formed along microshear zones in the host rock, during the initial state of the coseismic failure.

These quartz clasts (*qtz-1*) are mostly surrounded by a 0.2–1 μm thick rim (*qtz-2*) forming quartz spherulites (Fig. 13a–f). TEM–EDS (energy-dispersive spectrometry) element mapping (Fig. 13d), EDS compositional profiles (Fig. 13e) and BSE-SEM imaging (higher Z-contrast in Fig. 13a) all show an enrichment of Fe and Ti in the spherulitic *qtz-2* rim. Small inclusions of mica (mainly biotite, with a grain size up to 700 nm) and Ti-phases (ilmenite and rutile, with a grain size of 50–200 nm) are abundant in *qtz-2*. The inclusions within *qtz-2* mostly have a euhedral shape. Elongated to rounded ilmenite and rutile are often concentrated at the boundary between *qtz-1* and *qtz-2* (Fig. 11c-II), and/or at the outer surface of this spherulite rim (Fig. 13e, f). Muscovite and biotite flakes, commonly with rounded ends, are present as monomineralic flakes and sometimes as combined crystals (Fig. 13f).

The *qtz-2* rim surrounding single crystal *qtz-1* is monocrystalline and overgrows the core clast epitaxially. Radial growth of polycrystalline spherulitic rims occurs locally in the case of polycrystalline clasts (Fig. 12b-II). The spherulitic *qtz-2* rim around clasts is more pronounced in the centre of the thickest (>500 μm) portions of *fault$_{1+2}$* veins, within *fault$_3$* veins and injection veins (Fig. 12).

The *qtz-2* spherulites are in turn locally overgrown by an epitaxial rim of almost pure, inclusion-free quartz (*qtz-3*) (Figs. 12b-III and 13g). Only few dislocations are present within *qtz-3* (Fig. 13g, h). In areas of high spherulite density, the *qtz-3* rims of adjacent spherulites impinge against each others and build a mosaic aggregate (with a 2–5 μm grain size) with polygonal grains, cored by *qtz-2* spherulites, showing triple junctions at 120° (Fig. 12b-III and c-II). The grain boundaries of these spherulite-cored *qtz-3* aggregates are typically decorated with fluid inclusions (Figs. 12b-III, c-II and 13g, h). The formation of polygonal *qtz-3* fabrics mainly occurs within *fault$_3$* (Fig. 12b-III) and injection veins (Fig. 12c-II) and are rarely observed in *fault$_1$* veins.

5.2.2. Pseudotachylyte matrix

In the SEM-BSE images of Fig. 12a and b, at a relatively low magnification, three different domains can be distinguished: (i) dark-grey, coarse clasts of quartz, (ii) grey pseudotachylytes domains, including the coarse clasts, and (iii) irregular white patches. The grey areas of the pseudotachylyte correspond to domains volumetrically dominated by small quartz clasts overgrown by *qtz-2* rims (the trace amounts of Ti and Fe explains the lighter BSE grey level compared with the quartz clasts, Fig. 13a and d). Between the small quartz spherulites there is an interstitial matrix formed by K-feldspar + muscovite. The large white patches in the pseudotachylytes consist of K-feldspar (orthoclase, Kfsp, identified by EBSD pattern analysis). No compositional zoning of Kfsp is evident in the SEM-BSE images (Fig. 12b-I, c-I). EBSD analysis reveals that these patches consist of large (up to several 100's μm) skeletal single crystals grown within the dispersed cloud of quartz clasts and quartz spherulites (Fig. 14). TEM images show the presence of only few dislocations and the rare subgrain boundaries within the Kfsp (Fig. 13c). Kfsp contains small inclusions of zircon, apatite, Fe-sulfide and mica.

5.2.3. Pseudotachylyte vein structure

The ratio between clasts and matrix, their spatial distribution and their microstructures vary at different positions in a pseudotachylyte vein and between the different veins. The different fabric components (*qtz-1* clasts, *qtz-2* and *qtz-3* rims, and matrix) could be discriminated automatically by image analysis (see Section 2.6) of SEM-BSE photos by their different greyscale colours: (i) white-light grey for K-feldspar and muscovite, (ii) medium grey for impure *qtz-2* spherulitic rims, and (ii) dark grey for *qtz-1* clasts and *qtz-3* mosaic (not distinguishable by the applied image analyse method). Data were collected from mosaics of SEM-BSE images taken at 150× (image resolution 2048 × 1536) and 200× (image resolution 1026 × 624) magnification to allow a meaningful area to be analysed. A test of the reliability of the data collected in this way was made on mosaics of images with 500× magnification (3072 × 2304) taken from parts of the 200× magnification mosaic-area.

On average, the *fault$_{1+2}$* veins contain 21–25 vol.% *qtz-1*, 63–64 vol.% *qtz-2* and 11–13 vol.% K-feldspar (+muscovite) and 1–2 vol.% inclusions. *Qtz-3* rarely appears in *fault$_{1+2}$* veins. *Fault$_3$* veins contain 35–40 vol.% *qtz-1* and *qtz-3*, 43–49 vol.% *qtz-2*, 12–14 vol.% K-feldspar (+muscovite), and 1–2 vol.% inclusions.

A major difference between the *fault$_{1+2}$* veins and *fault$_3$* injection veins is the distribution and size of the K-feldspar matrix patches. The pseudotachylyte matrix appears strongly intermixed with the quartz domains in the *fault$_{1+2}$* veins, whereas *quartz-1-2-3* and K-feldspar form separate domains in the *fault$_3$* injection veins.

6. Discussion

6.1. Quartz melting in pseudotachylyte

The pseudotachylytes within the SNFZ quartzite provide unequivocal evidence of extensive friction-induced melting of quartz. In SNFZ pseudotachylytes, the volume of quartz spherulitic rims, crystallized from the melt, accounts for more than 60 and 40 vol. % in *fault$_{1+2}$* and *fault$_3$* veins, respectively. Considering that the host-rock contains up to 12 vol.% of muscovite (±1–2% K-feldspar), which to a first approximation corresponds to the volume fraction of K-feldspar ± muscovite in the matrix, the largest part of the melt must have been almost pure silica derived from the host quartz and cannot be ascribed to a process of fractionation (e.g. Warr and van der Pluijm, 2005). Extensive melting of quartz in tectonic pseudotachylytes is not usual and quartz is commonly reported as survivor clasts within the pseudotachylyte matrix. However, rounded and embayed clasts within the matrix have been reported as evidence of local partial melting (Boullier et al., 2001). Di Toro and

structure and local high dislocation density in the transition zone between host grain and recrystallized aggregate; (f) transition between a deformed host quartz remnant (lower right part), with characteristic subgrain structure/high dislocation density, and new small dislocation-free grains within the microshear zone, and (g) dislocation-free new polygonal grains forming a mosaic aggregate with straight grain boundaries forming typical triple junction at 120°; the enlargement [I, II] show arrays of voids (fluid inclusions) along straight grain boundaries. (h) SEM-OC image of a microshear zone (upper part) along the margin of pseudotachylyte veins (lower part). (i) SEM-BSE (atomic contrast) image of quartz clasts (undeformed, left, and polycrystalline ultrafine-grained aggregate of former deformed host-rock, centre) within the pseudotachylyte (the location of this site is marked in Figs. 5c and 12b): qtz = quartz; msc = muscovite; kfsp = K-feldspar. Note ultrafine-grained host-rock microshear zone in direct contact to pseudotachylyte vein (upper part of the image). The dashed rectangle marks the area analysed by EBSD (see Fig. 9b). (j) Detail of the microstructure (SEM-OC image) of clast marked in (i).

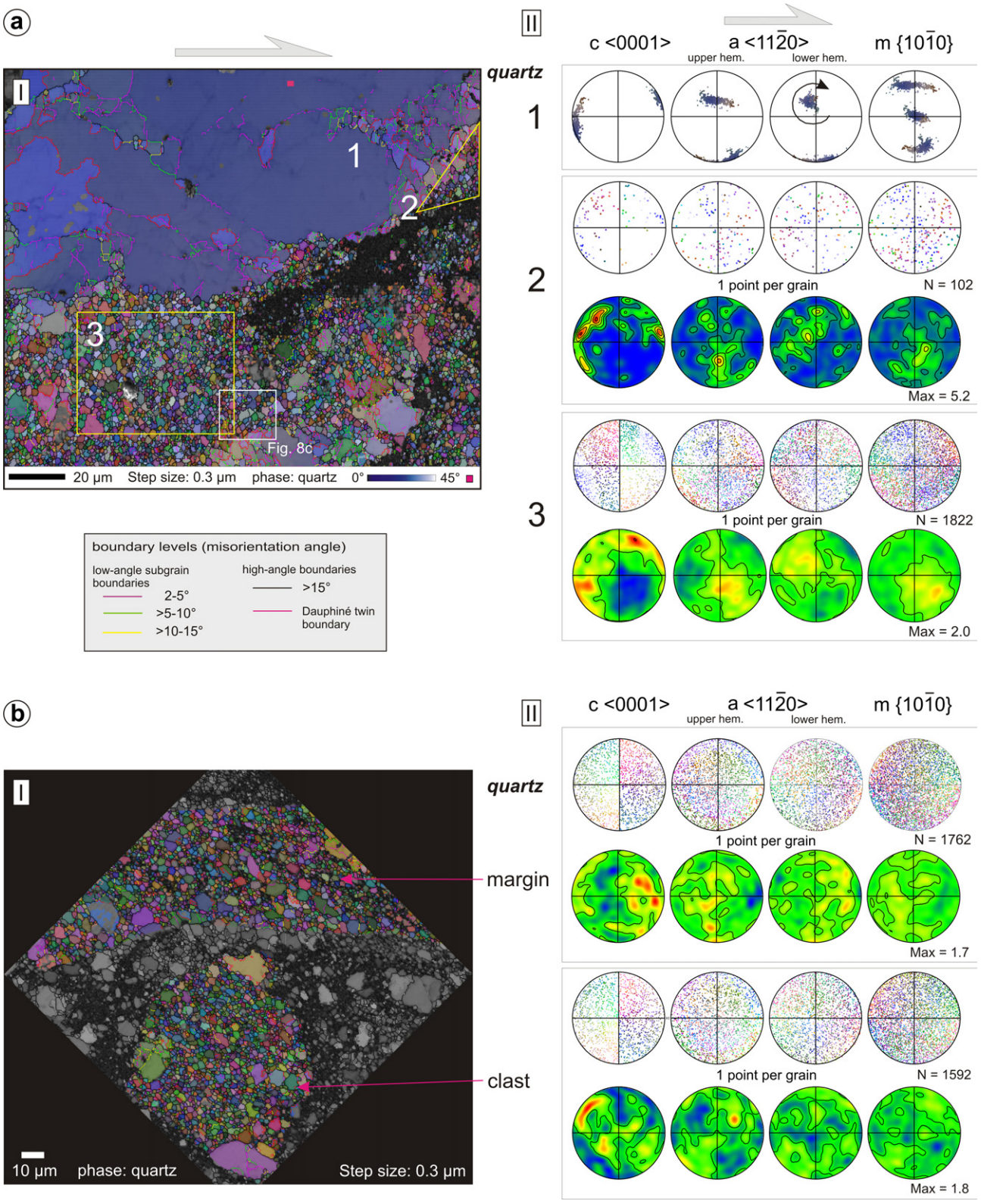

Fig. 9. EBSD analysis of quartz in (a) an intragranular microshear zone in the host quartzite (see location in Figs. 5d and 8a) and (b) along fault vein margin and, as a clast, within the pseudotachylyte (pt) vein (see location in Figs. 5c and 8i). [I] EBSD orientation maps; in the image each pixel is colour coded depending on quartz orientation (Euler angles). The substructure of host quartz in (a) is colour coded according to angular deviation from a given reference point (small red square in the upper part of the image). Boundary levels are colour-coded (see key). [II] Pole figures of <c>, <a> and <m> axes. For (a) the orientation data of the host domain (blue, area-1), small grains adjacent to the deformed host (area-2; one point per grain) and small grains within the intragranular deformation zone (area-3; one point per grain) are plotted; for (b) the data of the ultrafine-grained deformation zone in the host adjacent to the pt vein (margin, one point per grain) and the polycrystalline quartz clast within the pt vein are given (clast, one point per grain). The point colours in the plots are the same as in the EBSD maps. Note in (a-II) lattice distortion in the host grain indicates dextral shear sense (because antithetic *fault*$_3$ set) with a general rotation axis around one of the <a> axis of the host quartz. Pole figures are presented as equal area upper hemisphere stereoplots. In order to discriminate between $+a$ and $-a$ axes upper and lower hemisphere plots are presented for <11–20> direction. Multiples of random distribution (MRD) is colour coded in contoured pole figures (half width 15°, data clustering 5°). Red colour marks maxima, also given as numerical number (MRD).

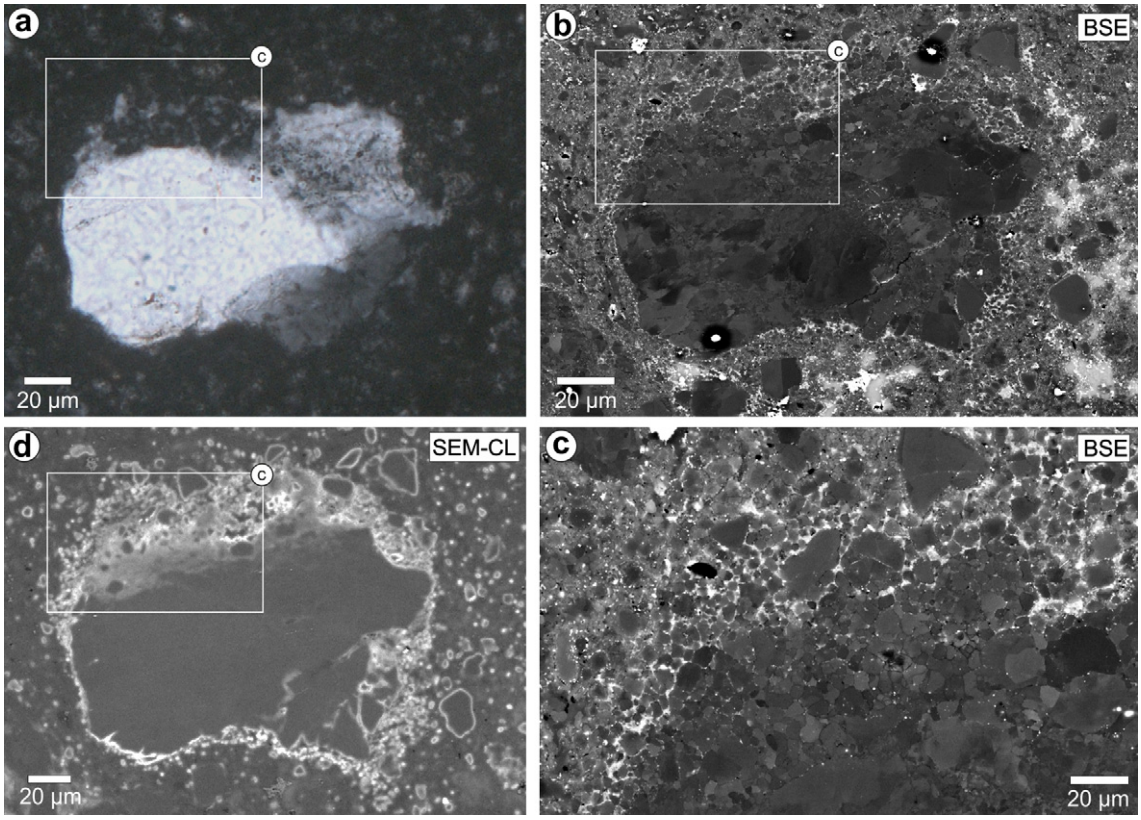

Fig. 10. Interaction between quartz clast and melt. (a) Optical micrograph (crossed polars) of a polycrystalline clast in *fault$_1$* vein. (b) BSE image of the same area as in (a). Note that the ultrafine-grained, recrystallized portion of the quartz clasts disaggregates into single grains along the grain boundaries at the periphery of the clast due to intrusion of melt, indicated by a K-feldspar-muscovite matrix (white box)(enlargement in (c)). In the BSE image: *qtz-1* is black to dark-medium grey (depending on the crystallographic orientation contrast – the used four-quadrant BSE detector produce, in addition to the Z-contrast, an orientation contrast signal), *qtz-2* is medium to light grey, and K-feldspar + muscovite is light grey–white medium grey. (d) SEM-CL image of the same area as in (a–b). The coarse-grained quartz clast shows a bright CL narrow rim. In the case of polycrystalline clast portions the bright CL signal is pervasive, even in the clast interior where there are only a sparse isolated small blebs of melt-derived pockets.

Pennacchioni (2004) showed that, in contrast to plagioclase, whose amount (total clast area) significantly decreases towards the centre of thick (>1 cm) pseudotachylyte veins, quartz remains approximately constant across the veins. This was interpreted as evidence that in the centre of the vein, where high melt temperatures lasted for a longer time, plagioclase was consumed by melting whereas quartz was not; the initial melt temperature was inferred to have been between 1200 °C (plagioclase single-phase melting under dry conditions) and 1720 °C (quartz single-phase dry melting) (Deer et al., 1992). It is to point out that none-equilibrated frictional melting during coseismic events predicts that melting only occurs at the melting temperature higher than that of each individual rock-forming mineral (Lin, 2008).

In the case of the SNFZ pseudotachylytes, melting of quartz should indicate a melt temperature of 1720 °C, assuming dry conditions (Deer et al., 1992). The absence of free water fluids, and fluid-deficient conditions in general, are a common assumption for pseudotachylytes (Spray, 1992). The effect of a free fluid phase along a fault plane during seismic slip would cause shear heating-induced thermal pressurization of the fault and a loss of frictional resistance (Sibson, 1973; Mase and Smith, 1987; Otsuki et al., 1999), precluding the onset of friction-induced melting. However, the assumption of dry conditions during pseudotachylyte generation is not probably always correct, as it is suggested by the coexistence of pseudotachylytes and epidote-chlorite veins at the contractional and extensional bends, respectively, of undulated fault surfaces within the Sierra Nevada (Griffith et al., 2010).

In the SNFZ quartzite, water fluids were certainly released during frictional melting of muscovite. Water was probably also present as a free fluid phase before coseismic slip, as abundant fluid inclusions present along the grain boundaries of ultrafine-grained recrystallized quartz of the microshear zones and, as trails, in the host coarse-grained quartz (Krenn, 2010). Fluids can be incorporated in a melt as dissolved volatiles and this would prevent thermal pressurization of the fault. Boullier et al. (2001) inferred about 8 vol. % of volatiles dissolved in the frictional melt on the basis of the EMPA-determined composition of the glassy matrix of pseudotachylytes within a granodiorite exhumed along the Nojima Fault (Japan). The presence of fluid inclusions in the Nojima pseudotachylyte glass provides evidence of H_2O and CO_2 saturation in the melt, originating from melting of H_2O-bearing minerals and carbonates. Thus potentially a relatively large amount of fluids can be stored in the melt, although fluid solubility in a melt is largely dependent on melt composition and on pressure.

Under the same ambient conditions, muscovite has a lower single-mineral melting temperature than quartz (ca. 1300 and 1720 °C, respectively, under dry conditions) and should undergo melting at an earlier stage according to the general assumption for pseudotachylytes of non-equilibrium (non-eutectic) fusion (Lin, 2008). In the SNFZ pseudotachylytes, this is supported by the observation that within clasts of the former compact ultrafine-grained recrystallized quartz the grain boundary network was filled with K-feldspar + muscovite (Figs. 11b and b-I) mainly derived by muscovite melting. At that intial stage of coseismic frictional sliding, there is no clear microstructural evidence of involvement of quartz in melting (see also section 6.2). Therefore, water fluids produced by muscovite melting could have been incorporated in

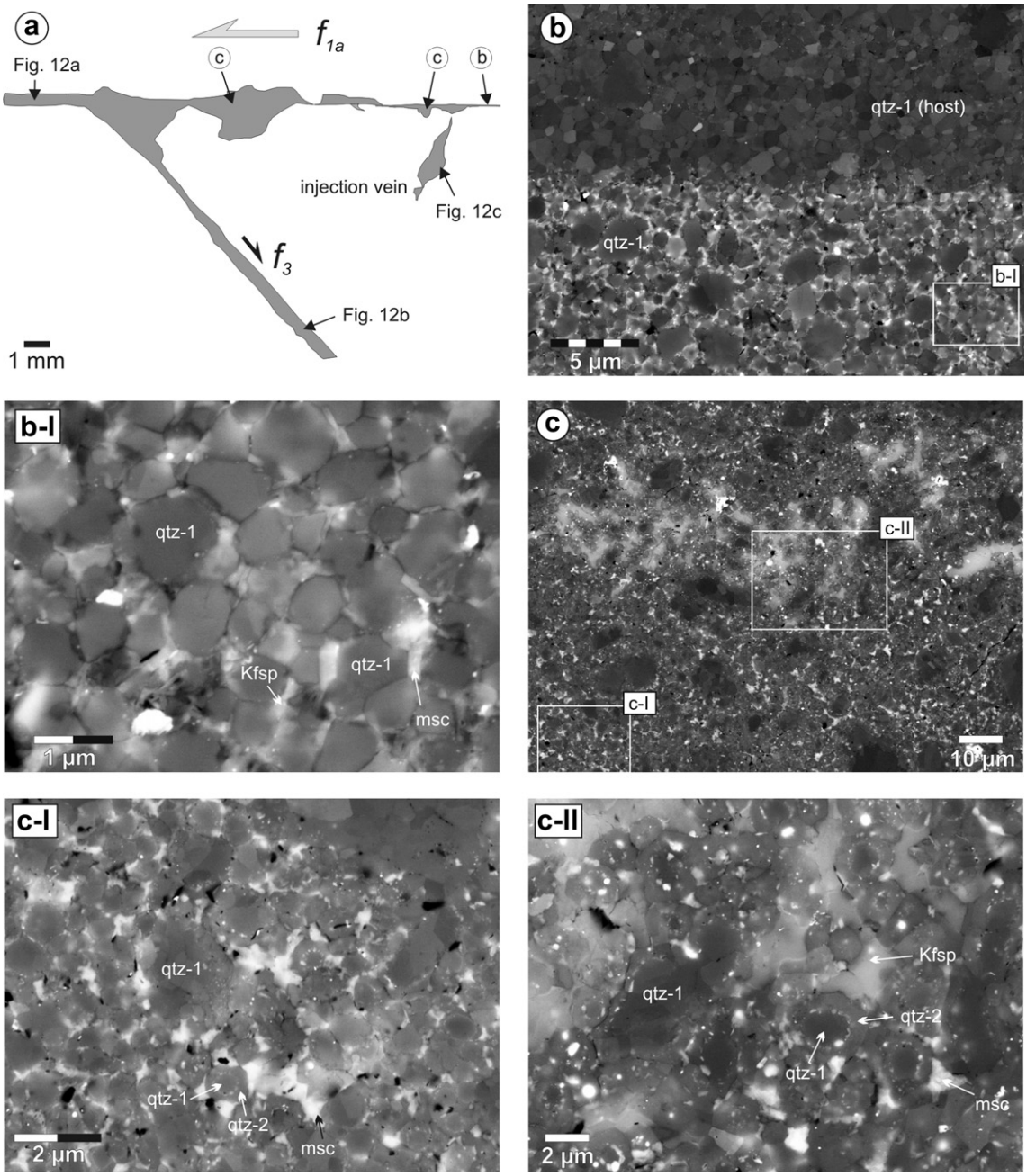

Fig. 11. Microstructural inventory of pseudotachylyte veins. (a) Sketch of *fault*$_{1+3}$ veins (simplified from Fig. 5a and e) and location of BSE images of (b–c) and Fig. 12. (b) Ultrafine recrystallized aggregate in the host quartzite (upper part) with a sharp contact with a pseudotachylyte vein (lower part) mainly formed of a dense population of quartz clasts, of a comparable grain size as the small grains in the wall rock, and an interstitial K-feldspar + muscovite matrix. (b-I) Detail of the microstructure in the pseudotachylytes. Quartz grains do not show any evident overgrowth. Kfsp = K-feldspar; msc = muscovite. (c) Heterogeneous microstructure in the pseudotachylytes including irregular domains dominated by K-feldspar matrix and clast-dominated portions with subordinate interstitial K-feldspar + muscovite. (c-I) Detail of a clast-dominated domain showing quartz clasts surrounded by spherulitic rims (*qtz-2*) enhanced by the lighter grey (due to a change in Fe and Ti composition, see Fig. 13) than the *qtz-1* cores and by the presence of concentrations of bright inclusions (Fe, Ti phase, see Fig. 13) at the interface between *qtz-1* and *qtz-2*. (c-II) Detail of a matrix-rich domain showing small quartz spherulites embedded in the Kfsp ± msc matrix.

part into the early K-rich melt before the occurrence of extensive quartz melting. Fluids present along the quartz grain boundaries could also have been dissolved in the early melt during fluid percolation through grain boundaries of (ultra)fine aggregates. As a result, some degree of hydrated conditions during melting, and consequently lower temperature of fusion of single minerals than under dry conditions, can be reasonably assumed during seismic slip in the SNFZ quartzite. For example, the melting point of quartz can vary from 1100 to1720 °C, depending on both water activity and pressure (Kennedy et al., 1962). The first melting of quartz is documented by the appearance of rounded small quartz clasts and embayed coarser quartz clasts (e.g. Sibson, 1975; Lin, 1999; Magloughlin, 1992) (Fig. 11c-I). Subsequently, these clasts act as nuclei for concentric growth of impure secondary quartz (*qtz-2*) from a quartz-rich melt (Sato, 1975; Macaudiére et al., 1985; Lin, 1994) (see also section 6.2). Hydrated conditions during crystallization of quartz are also suggested by the crystallization of biotite/muscovite, forming small idioblastic inclusions in the spherulitic *qtz-2* rims (Fig. 13e, f) and by fluid inclusions along the *qtz-3* grain boundary network (Fig. 12b-III and 13h).

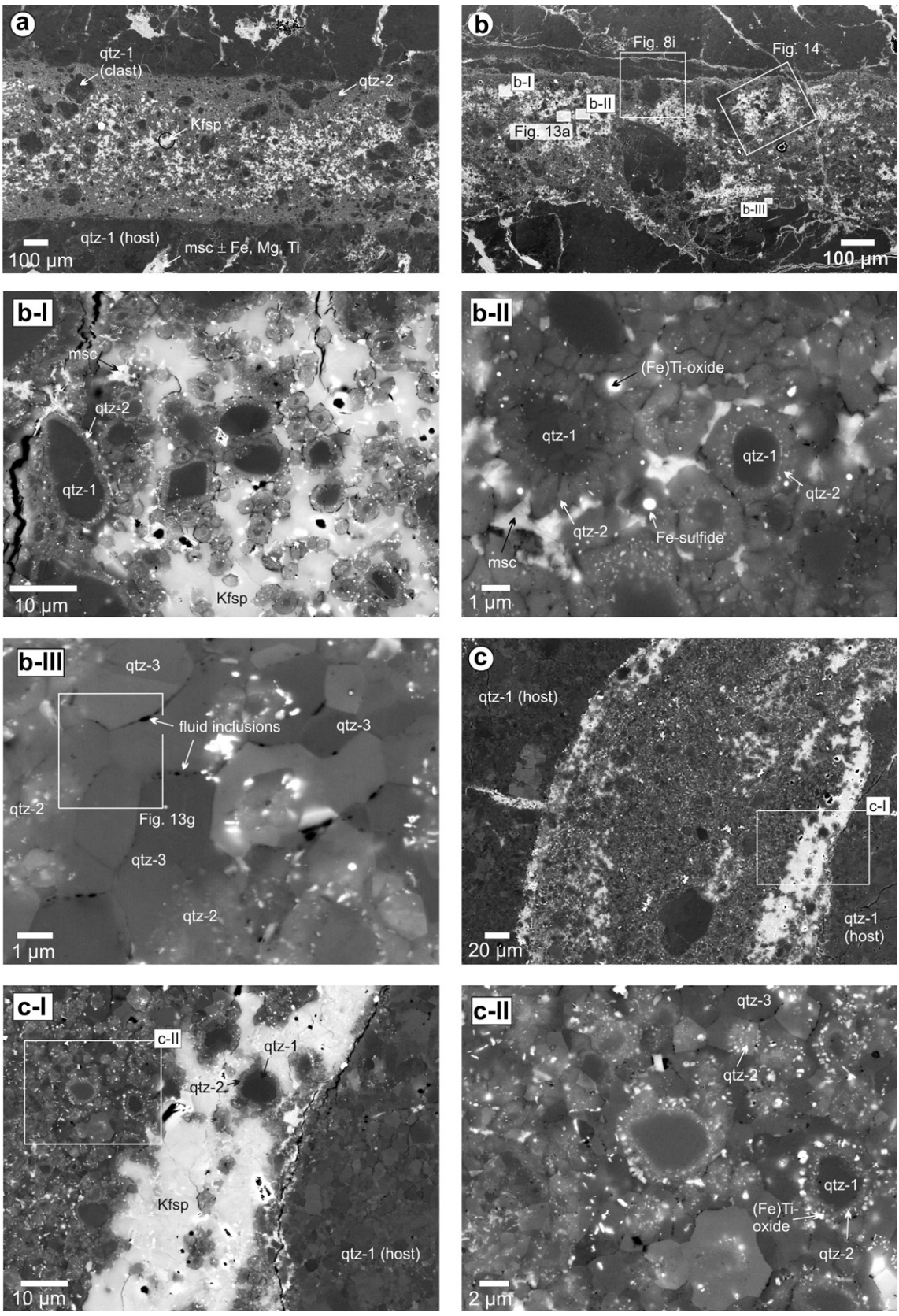

Fig. 12. Inventory of BSE microstructural images from (a) *fault*$_1$, (b) *fault*$_3$ and (c) injection veins. (a) Overview of *fault*$_1$. (b) Overview of *fault*$_3$. (b-I) Spherulitic quartz clasts (*qtz-1* + *qtz-2*) floating in a locally homogeneous Kfsp matrix. (b-II) Polycrystalline spherulitic rim of radially distributed *qtz-2* crystals surrounding a polycrystalline quartz-1 clasts and monocrystalline spherulite around single grain clasts. (b-III) Mosaic fabric of equate, inclusion-free impinging *qtz-3* overgrowths. Note the presence of small fluid inclusions (dark dots) along the grain boundaries. (c) Zoned pseudotachylyte injection vein including a quartz (*qtz-1* + *qtz-2*) spherulite-dominated interior and a Kfsp matrix-dominated zone at the contact with the wall rock. (c-I) Detail of the sharp contact between quartz spherulite-dominated domain (inner vein) and the Kfsp matrix-dominated domain (vein border). (c-II) Detail of *qtz-1-3* aggregate in the Kfsp matrix-free pseudotachylyte inner domain.

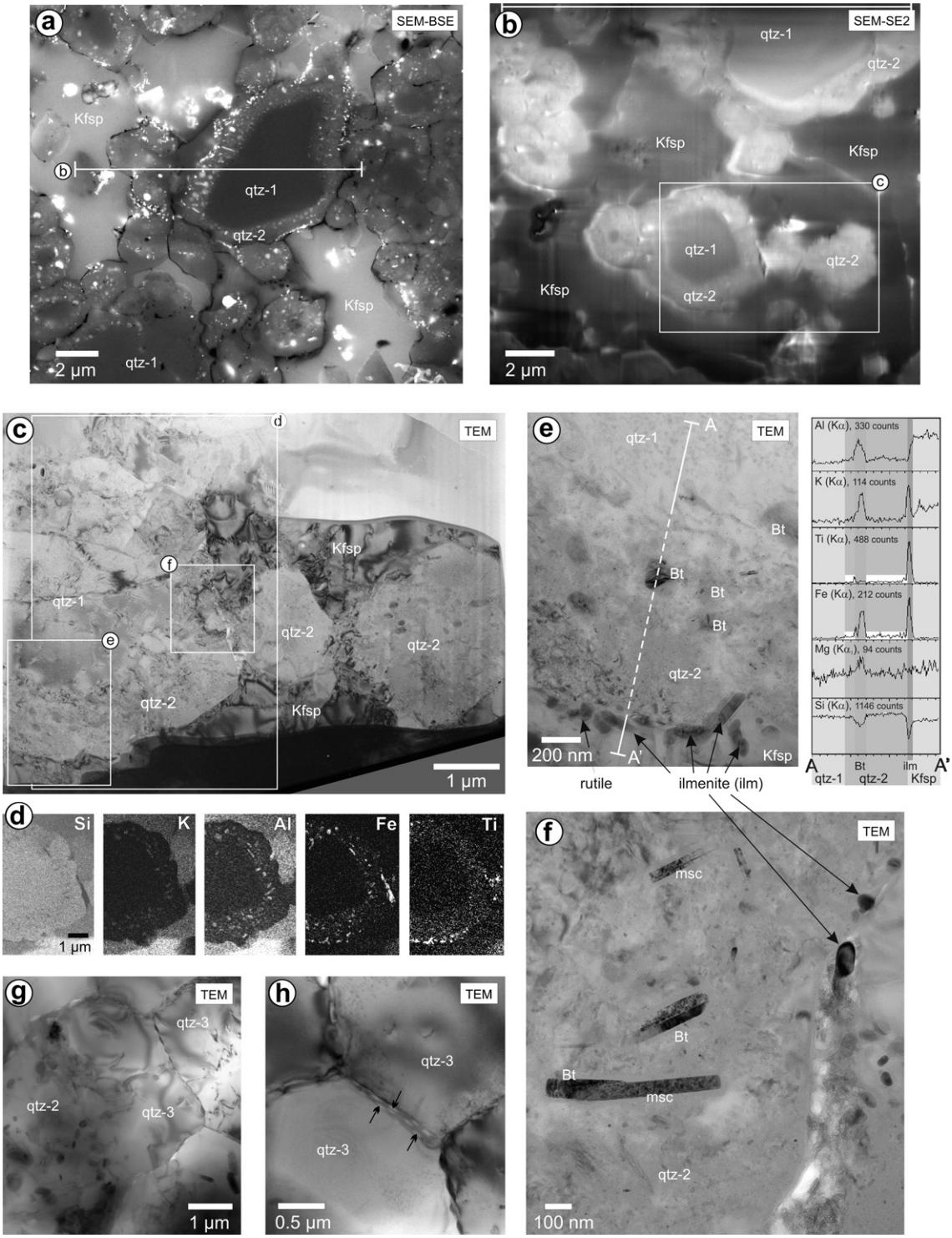

Fig. 13. (a–f) Microstructural and geochemical analysis of quartz spherulites within Kfsp matrix, marked in Fig. 12b. (a) SEM-BSE image showing the sectional line (white), along which the TEM-lamellae was prepared, across quartz spherulites in a K-feldspar matrix. (b) Compositional contrast image obtained with SEM–SE2 detector of the TEM lamellae. (c) TEM (bright field) image of the area marked in (b) showing the quartz spherulites within the Kfsp matrix. Note Kfsp matrix shows only few dislocations. (d) TEM–EDS (energy-dispersive spectrometry) element maps of spherical quartz spherulite. (e) Element (EDS) profile across quartz spherulite (*qtz-1* and *qtz-2*). Note slightly enhanced content of Ti and Fe within *qtz-2* as marked along stippled line in the TEM image and as white area in the Ti and Fe element line profiles. (f) Microlite inclusions of biotite (Bt), muscovite (msc) within and ilmenite at the margin of *qtz-2*. (g) TEM microstructure of *qtz-2* and *qtz-3* developed within *fault*$_3$ vein. Note *qtz-2* contains inclusions whereas *qtz-3* is "pure" quartz. (h) Fluid inclusions (black arrows) along the grain boundaries of *qtz-3*.

The occurrence of extensive quartz melting in the SNFZ pseudotachylyte prompts the question as to why quartz melting is rarely reported in other pseudotachylytes. The process of quartz melting can be overlooked or difficult to detect in pseudotachylytes within polycrystalline rocks (especially in the ultrafine-grained clast fraction), but it is a common observation that quartz is mainly preserved as a clast in pseudotachylyte. The common interpretation is that quartz has a high single-mineral melting temperature and, under

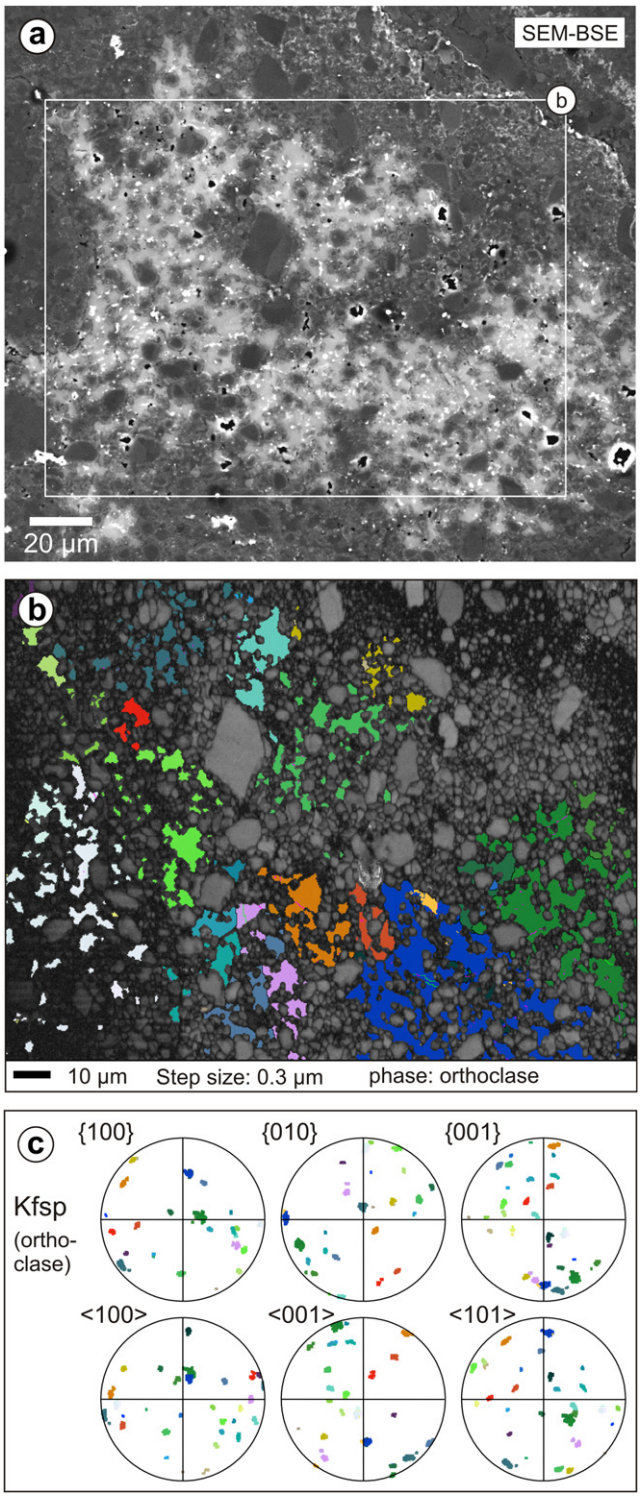

Fig. 14. EBSD analysis of the K-feldspar fabric of the pseudotachylyte martrix. (a) SEM-BSE image of the analysed area within a *fault*$_3$ vein (location is shown in Fig. 12b). (b) EBSD orientation map of Kfsp matrix. Note that the matrix consists of large (several 10s of microns) amoeboid single crystals of different orientation. Note subgrain boundaries are rare. (c) Pole figures of Kfsp crystallographic orientation. Figure description for EBSD data presentation follows those for Fig. 9.

the commonly assumed almost dry conditions in pseudotachylytes, it would escape melting even in superheated melts (Di Toro and Pennacchioni, 2004). As discussed above, the SNFZ quartzite initially contained water fluids and water-bearing phases, and melting under hydrous conditions can dramatically lower the melting temperature of quartz and other minerals. However, friction-induced melting in rock containing hydrous mineral phases (and thus capable of releasing aqueous fluids during coseismic faulting), as well as intragranular and grain boundary fluid inclusions, appears to be common rather than the exception. Many pseudotachylytes are preceded by cataclastic deformation (Magloughlin, 1992), which is commonly associated with a large fluid influx and rock alteration (Boullier et al., 2001; Di Toro and Pennacchioni, 2004; Caggianelli et al., 2005). Another explanation for the limited quartz melting in quartz-bearing polymineralic rock is that the melting of large amounts of minerals with a lower melting point than quartz buffers the friction melt temperature due to latent heat of fusion. This would impede the temperature rise until the complete consumption of these minerals. For example, the tonalite described by Di Toro and Pennacchioni (2004) consists of plagioclase (45–50% in volume), quartz (25–30%), biotite (15–20%) and K-feldspar (1–5%) and consequently a large amount of the total frictional heat generated along the fault plane must have been used for the complete melting of >70% of the rock volume before the temperature could rise to the melting point of quartz. In contrast, after consumption of the minor volume of muscovite in the SNFZ quartzite, heat was readily available to increase temperature. Therefore, under similar ambient conditions and amount of coseismic slip, quartz melting is more likely effective in a quartzite than in quartz-bearing crustal rocks. The validity of this speculation is difficult to assert, given the non-equilibrium character of friction-induced melting.

6.2. Immiscible friction-induced melts

The SNFZ pseudotachylytes show two distinct components derived from crystallization of the friction-induced melts, namely: the K-feldspar ± muscovite matrix and the *qtz-2* and *qtz-3* overgrowths of *qtz-1* clasts. These two melt-derived components developed at different stages in the friction-induced melting process and represent distinct, immiscible melts. The former developed at an earlier stage due to melting of muscovite that underwent complete fusion in the frictional melt. This is suggested by the incipient filling of pore space and dilatants grain boundaries of the clasts of ultrafine-grained quartz with K-feldspar and muscovite; at this stage of pseudotachylyte evolution, there is no evidence of development of any *qtz-2* rim in the "melt-infiltrated" aggregate (Fig. 11b and b-I). The absence of transitional domains with an intermediate composition indicates that the K-rich and silica-rich melts were almost immiscible. However some "contamination" of the quartz melt is indicated by the presence of the widespread small (50–200 nm) biotite/muscovite, ilmenite and rutile inclusions preserved in the spherulitic rims, together with the Ti- and Fe-enriched *qtz-2* composition (Fig. 13d, e, f). The local overgrowth of *qtz-2* spherulites by an almost pure inclusion-free quartz-3 fabric gives evidence that quartz melt changed composition with time. These *qtz-3* overgrowths mainly developed along *fault*$_3$ zones and injection veins, whereas they appear absent along the main fault$_1$ veins where melts underwent pervasive shearing, flow and mechanical mixing after formation.

The size and the rounded shape of ilmenite and rutile inclusions within the *qtz-2* rims and in contact to the *qtz-3* overgrowth seems to exclude that they are fragments derived from the host-rock. Instead, the concentrations of Fe- and Ti-rich minerals within the *qtz-2* rims are considered to have formed by the preferential fractional crystallization of mafic minerals from the melt (Warr and van der Pluijm, 2005). Geochemical TEM analysis reveals that a small amount of Ti and Fe (Fig. 13e) are also incorporated into the *qtz-2* lattice, which is why *qtz-2* appears medium grey in electron

backscatter images. The concentration of idioblastic inclusions of ilmenite and rutile at the inner or outer part of *qtz-2* rim, with respect of the position of the spherulites within the fault veins, indicates an early and late state of preferred crystallization of the Fe–Ti phases from the melt. Ti and Fe could be released during melting of muscovite, which contains 2–7 wt.% FeO and up to 2.6 wt.% TiO_2. Melting of the Fe–Ti ore phase from the host-rock could also be a source for Fe and Ti. This would imply friction-induced melting points of 1356 °C for ilmenite, 1475–1565 °C for hematite and 1825 °C for rutile.

6.3. Ductile microshear zones associated with pseudotachylyte

Pseudotachylytes are spatially associated with microshear zones in the host-rock showing recrystallization of quartz to ultrafine-grained aggregates. The host-rock coarse quartz grains adjacent to the microshear zones show deflection and reorientation of the lattice around rational crystallographic axes (Fig. 9a), typical of crystal plastic deformation and dislocation creep (Lloyd and Freeman, 1994; Lloyd et al., 1997; Prior et al., 2002; Bestmann and Prior, 2003; Bestmann et al., 2008). The dislocation substructures are also indicative of crystal-plasticity. The development of a subgrain mosaic with partly well-ordered dislocations walls (Fig. 8e) adjacent to areas with a high dislocation density (with a low degree of organization) indicates that both dislocation creep and dislocation glide took place. The small new grains adjacent to strongly deformed host-rock quartz have a crystallographic orientation slightly misoriented with respect to that of the host and show a dispersion around rational axes close in orientation to the Y-axis (the vorticity axis of bulk deformation). The grain size of new grains is of the same order of magnitude as the subgrain size in the host. These features would be consistent with subgrain rotation recrystallization. In detail, the new recrystallized grains are slightly coarser (0.5–2 μm) than the subgrains (0.3–0.5 μm) in the parent quartz, probably due to post-kinematic static grain growth. As a result, an equilibrated grain boundary network of strain free new grains within the microshear zones developed (Fig. 8d, g).

The randomization of the CPO of the new small grains within the microshear zone (Fig. 9a) might be related to the activity of grain-size-sensitive (GSS) grain boundary sliding, subsequent to grain size reduction by subgrain rotation recrystallization (De Bresser et al., 2001; Bestmann and Prior, 2003). Thus we infer that new recrystallized grains, once formed, are able to deform and rotate by grain boundary sliding and cause a weakening of the former existing CPO (Casey and McGrew, 1999; Bestmann et al., 2008).

A detailed discussion about the significance of the plastic deformation mechanism within the quartzites associated with coseismic faulting will be published elsewhere. We will compare the crystal plastic microfabrics (microstructure and CPO) of these pseudotachylyte-related shear zones with microfabrics interpreted as the result of short-term deformation at high stress in the (semi) brittle regime and subsequent stress release (Trepmann and Stöckhert, 2003; Trepmann et al., 2007). In this interpretation, recrystallization and the annealed microstructure of quartz aggregates is mainly the result of (dynamic and/or static) recovery of the highly-distorted and dislocation-rich portions of quartz involved in transient low-temperature crystal-plasticity developed during downward propagation of earthquake ruptures to the upper ductile crust.

6.4. Timing of host-rock deformation and pseudotachylyte development

The *fault*$_{1-3}$ pseudotachylytes strictly follow a precursor network of localized microshear zones characterized by strong grain size reduction. Once formed, these deformed zones were preferentially used as slip surfaces during coseismic slip. The aggregates of ultrafine-grained microshear zones are present in the host quartzite at the contact or at a small distance from pseudotachylyte and are included as clasts within the veins. This indicates a phase of localized plastic deformation prior to the formation of the pseudotachylytes. The kinematics of deformation in the microshear zones (constrained by EBSD data, Fig. SOM1) is consistent with both the general top-to-NW sense of shear in the high temperature fabric of the SNF (Sölva et al., 2005; G. Cotza, personal comment) and the sense of shear during the coseismic faulting generating the pseudotachylyte veins (constrained by flow fabrics, Fig. 7a and Fig. SOM4).

The question arises of whether the ultrafine aggregates developed at different ambient (P, T) conditions than coseismic slip, during a separate, pre-existing deformation phase, or during a precursory, almost coeval stage to the pseudotachylytes-generating event and thus belong to the seismic cycle. The actual time lapse between pre-seismic crystal plastic grain size reduction and coseismic rupture process is difficult to constrain. However, the following microstructural observations point to a continuous pre- to coseismic crystal plastic deformation of quartzitic host-rock material: (i) the development of melt pockets along *fault*$_1$ planes is controlled by microshear zones where the displacement-related opening space is directly filled with pseudotachylyte material (Fig. 5b and Figs. SOM2 and SOM3), (ii) the distorted and folded quartz host foliation near the main pseudotachylyte-bearing fault planes shows the same crystal plastic deformation microstructures (Fig. 6) and (iii) flow structures of deformed host quartz aggregates within pseudotachylyte veins are characterized by the same crystal plastic induced grain size reduction processes and microstructures (Fig. SOM4).

Recently, high-velocity rotary shear experiments on calcite Carrara marble at coseismic slip rates have produced similar microstructures as described here for the SNFZ pseudotachylytes. The marble also show a plastic deformation of the wall rock (bent calcite deformation twins accompanied by patchy undulose extinction) and a layer of ultrafine-grained (2–5 μm) calcite aggregates with equilibrated grain boundaries adjacent to the principal slip layer (Figure DR5 in Kim et al., 2010).

Our observations suggest that the fault-related plastic deformation microstructures of the pseudotachylyte-bearing SNFZ quartzite were coseismic and related to heterogeneous slip and strain rates during a single seismic event, consistently with the experimental observation of Kim et al. (2010). This could have occurred during the acceleration stages of the seismic faulting or by strain rate partitioning in host rock during the coseismic slip along the principal pseudotachylyte-bearing plane.

Post-seismic deformation can be excluded since, within the pseudotachylyte veins, neither the K-feldspar nor the *qtz-2* and *qtz-3* aggregates (both crystallized form the friction-induced melt) show any internal deformation microstructure (Fig. 13c, g, h). Even minor reactivation deformation or recrystallization would have overprinted these nearly dislocation-free microstructures. Thus neither host-rock nor coexisting pseudotachylyte veins show evidence of a multiphase deformation history.

7. Conclusions

During a single-jerk seismic event, pseudotachylyte veins developed at coseismic slip rates in the muscovite-bearing quartzite of the SNFZ (Southern Tirol, Italy) with extensive melting of quartz. During the same faulting event, crystal plastic deformation in the host-rock produced ultrafine-grained microshear zones.

Microstructural analysis provides unambiguous evidence of extensive quartz melting. This does not necessarily indicate melt temperatures as high as 1720 °C (quartz melting temperature under dry conditions), since partially hydrated conditions prevailed during coseismic faulting. Quartz melting in quartzite may be more common than in polymineralic rocks (e.g. granitoids) because of thermal buffering by the latent heat of fusion of the low-melting point minerals. In fact, quartz has one of the highest melting points of the common silicate rock-forming minerals.

The occurrence of pseudotachylytes in quartzite suggests that the fault-weakening mechanism in quartz described in experiments (Di Toro et al., 2004) at low confining pressure may be non-operative at deeper structural levels in the continental crust where large earthquakes nucleate and most pseudotachylytes are produced.

Pseudotachylytes are closely associated with crystal plastic deformation of the quartzitic host rock along microshear zones close to the fault plane. This deformation occurred before and during the main seismic slip along the pseudotachylyte-producing faulting. The development of localized plastic deformation during the seismic cycle deserves future investigation for a better understanding of the mechanics of earthquake sources.

Acknowledgment

The authors gratefully acknowledge: Gianluca Cotza for providing the sample and sample location; Ulli Exner for field support; Jens Schaufler, Elmar Schweitzer, Matthias Bickermann, Edeltraut Völkel and Florian Heidelbach for electron microscopy support; Volker von Seckendorf, Nico Langenhof and Jürgen Gose for microprobe support; Jens Götze and Rolf Neuser for HOT-CL support; Hubert Schulze, Angela Halfpenny, Werner Langer, Petra Rosner and Friederike Urban for sample preparation; Bernhard Grasemann, Gerlinde Habler, Bernhard Schulz, Bernhard Stöckhert, Claudia Trepmann and Markus Ebner for discussion; Hugh Rice for English correction; Claudia Trepmann and Aiming Lin for reviewing the manuscript. Further acknowledgments go to the Deutsche Forschungsgemeinschaft (DFG) for funding the project WA 1010/11-1 (Lab and research funding)(MB) and for supporting within the framework of its `Excellence Initiative' the Cluster of Excellence `Engineering of Advanced Materials' (www.eam.uni-erlangen.de) at the University of Erlangen-Nuremberg (MG). GP thanks Fondazione Cariparo (Progetto di eccellenza "Revealing the secrets of an earthquake: physico-chemical constraints from a multidisciplinary study of exhumed faults") and ERC StG 205175 for financial support.

Appendix. Supplementary data

Supplementary data related to this article can be found online at doi:10.1016/j.jsg.2010.10.009.

References

Adams, B.L., Wright, S.I., Kunze, K., 1993. Orientation imaging: the emergence of a new microscopy. Metallurgical Transactions 24A, 819–831.
Allen, A.R., 1979. Mechanism of frictional fusion in fault zones. Journal of Structural Geology 1, 231–243.
Bell, I.A., Wilson, C.J.L., McLare, A.C., Etheridge, M.A., 1986. Kinks in mica: role of dislocation and (001) cleavage. Tectonophysics 127, 49–65.
Bestmann, M., Prior, D.J., 2003. Intragranular dynamic recrystallization in naturally deformed calcite marble: diffusion accommodated grain boundary sliding as a result of subgrain rotation recrystallization. Journal of Structural Geology 25, 1597–1613.
Bestmann, M., Habler, G., Heidlebach, F., Thöni, M., 2008. Dynamic recrystallization of garnet and related diffusion processes. Journal of Structural Geology 30, 777–790.
Bossière, G., 1991. Petrology of pseudotachylytes from the Alpine fault of New Zealand. Tectonophysics 196, 173–193.
Boullier, A.-M., Ohtani, T., Fujimoto, K., Ito, H., 2001. Fluid inclusions in pseudotachylytes from the Nojima fault, Japan. Journal of Geophysical Research 106, 21965–21977.
Caggianelli, A., de Lorenzo, S., Prosser, G., 2005. Modelling the heat pulses generated on a fault plane during coseismic slip: inferences from the pseudotachylites of the Copanello cliffs (Calabria, Italy). Tectonophysics 405, 99–119.
Camacho, A., Vernon, R.H., Fitz Gerald, J.D., 1995. Large volumes of anhydrous pseudotachylyte in the Woodroffe Thrust, eastern Musgrave ranges, Australia. Journal of Structural Geology 17, 371–383.
Casey, M., McGrew, A.J., 1999. One-dimensional kinematic model of preferred orientation development. Tectonophysics 303, 131–140.
De Bresser, J.H.P., Ter Heere, J.H., Spiers, C.J., 2001. Grain size reduction by dynamic recrystallization: can it result in major rheological weakening. International Journal of Earth Sciences (Geologische Rundschau) 90, 28–45.
Deer, W.A., Howie, R.A., Zussman, J., 1992. An Introduction to the Rock Forming Minerals. Longman Scientific and Technical, pp. 696.
Di Toro, G., Pennacchioni, G., 2004. Superheated friction-induced melts in zoned pseudotachylytes within the Adamello tonalites (Italian Southern Alps). Journal of Structural Geology 26, 1783–1801.
Di Toro, G., Pennacchioni, G., 2005. Fault plane processes and mesoscopic structure of a strong-type seismogenic fault in tonalites (Adamello batholith, Southern Alps). Tectonophysics 402, 54–79.
Di Toro, G., Goldsby, D.L., Tullis, T.E., 2004. Friction falls towards zero in quartz rock as slip velocity approaches seismic rates. Nature 427, 436–439.
Di Toro, G., Pennacchioni, G., Teza, G., 2005. Can pseudotachylytes be used to infer earthquake source parameters? an example of limitations in the study of exhumed faults. Tectonophysics 402, 3–20.
Di Toro, G., Pennacchioni, G., Nielsen, S., 2009. Pseudotachylytes and earthquake source mechanisms. In: Fukuyama, E. (Ed.), Fault-zone Properties and Earthquake Rupture Dynamics. International Geophysics Series, vol. 94. Elsevier, pp. 87–133.
Frey, M., Desmons, J., Neubauer, F., 1999. The New Metamorphic Map of the Alps, EUG 10. Terra Abstracts. Cambridge Publications, Strassbourg, pp. 792.
Griffith, W.A., Nielsen S., Di Toro G., Smith S.A.F., 2010. Rough faults, distributed weakening, and off-fault deformation. Journal of Geophysical Research 115, B08409, pp. 1–22.
Habler, G., Sölva, H., Thöni, M., 2006. Tracing the high pressure stage in the polymetamorphic Texel Complex (Austroalpine basement unit, Eastern Alps): P-T-t-d constraints. Mineralogy and Petrology 88, 269–296.
Hoinkes, G., Thöni, M., 1987. New findings of eclogites within the eo-Alpine amphibolite grade area of the Ötztal basement. Terra Cognita 7, 96.
Kennedy, G.C., Wasserburg, G.J., Heard, H.C., Newton, R.C., 1962. The upper three-phase region in the SiO–H_2O. American Journal of Science 260, 501–521.
Kim, J.-W., Ree, J.-H, Han, R., Shimamoto, T., 2010. Experimental evidence for the simultaneous formation of pseudotachylyte and mylonite in the brittle regime. Geology 38, 1143–1146.
Konzett, J., Hoinkes, G., 1996. Paragonite-hornblende assemblages and their petrological significance: an example from the Austroalpine Schneeberg Complex, Southern Tyrol; Italy. Journal of Metamorphic Geology 14, 85–101.
Krenn, K., 2010. Fluid inclusions in quartz related to subsequent stages of foliation development during a single metamorphic cycle (Schneeberg Fault Zone, Eastern Alps, Austria). Lithos 118, 255–268.
Lin, A., 1994. Microlite morphology and chemistry in pseudotachylite, from the Fuyun fault zone, China. Journal of Geology 102, 317–329.
Lin, A., 1999. Roundness of fragments in pseudotachylytes as an indicator of frictional melting. Journal of Structural Geology 21, 473–478.
Lin, A., 2008. Fossil Earthquakes: The Formation and Preservation of Pseudotachylytes. In: Lecture Notes in Earth Sciences, vol. 111. Springer, pp. 348.
Lloyd, G.E., Freeman, B., 1994. Dynamic recrystallization of quartz and quartzites. Journal of Structural Geology 16, 867–881.
Lloyd, G.E., Farmer, A.B., Mainprice, D., 1997. Misorientation analysis and the formation and orientation of subgrain and grain boundaries. Tectonophysics 279, 55–78.
Macaudiére, J., Brown, W.L., Ohnenstetter, D., 1985. Microcrystalline textures resulting from rapid crystallization in a pseudotachylite melt in a meta-anorthosite. Contribution of Mineralogy and Petrology 89, 39–51.
Maddock, R.H., 1983. Melt origin of fault-generated pseudotachylytes demonstrated by textures. Geology 11, 105–108.
Maddock, R.H., 1986. Partial Melting of Lithic Porphyroclasts in Fault-Generated Pseudotachylytes, vol. 155. Neues Jahrbuch für Mineralogie, Abhandlungen, 1–14.
Maddock, R.H., 1992. Effects of lithology, cataclasis and melting on the composition of fault-generated pseudotachylytes in Lewisian gneiss, Scotland. Tectonophysics 204, 261–278.
Magloughlin, J.F., 1989. The nature and significance of pseudotachylite from the Nason terrane, North Cascade Mountains, Washington. Journal of Structural Geology 11, 907–917.
Magloughlin, J.F., 1992. Microstructural and chemical changes associated with cataclasis and frictional melting at shallow crust levels: the cataclasite-pseudotachylyte connection. Tectonophysics 204, 243–260.
Mancktelow, N.S., Pennacchioni, G., 2004. Microstructures of quartz mylonites: the importance of grain boundary fluids. Journal of Structural Geology 26, 47–69.

Mase, C.W., Smith, L., 1987. Effects of frictional heating on the thermal, hydrologic, and mechanical response of a fault. Journal of Geophysical Research 92 (B7), 6249–6272.

Otsuki, K., Monzawa, N., Nagase, T., 1999. Thermal pressurization, fluidization and melting of fault gouge during seismic slip recorded in the rock from Nojima fault. In: Ito, H., et al. (Eds.), International Workshop of the Nojima Fault Core and Borehole Data Analysis. Geological Survey of Japan, Tsukuba, pp. 43–50.

Prior, D.J., Wheeler, J., Peruzzo, L., Spess, R., Storey, C., 2002. Some garnet microstructures: an illustration of the potential of orientation maps and misorientation analysis in microstructural studies. Journal of Structural Geology 24, 999–1011.

Sato, H., 1975. Diffusion coronas around quartz xenocrysts in andesite and basalt from Tertiary volcanic region in northeastern Shikoku, Japan. Contributions to Mineralogy and Petrology 50, 49–64.

Schmidt, N.H., Bildesorensen, J.B., Jensen, D.J., 1991. Band positions used for online crystallographic orientation determination from electron back scattering patterns. Scanning Microscopy 5, 637–643.

Sibson, R.H., Toy, V., 2006. The habitat of fault-generated pseudotachylyte: presence vs. absence of friction melt. In: Abercrombie, R., McGarr, A., Di Toro, G., Kanamori, H. (Eds.), Earthquakes: Radiated Energy and the Physics of Faulting. Geophysical Monograph Series, vol. 170. American Geophysical Union, Washington, DC, pp. 153–166.

Sibson, R.H., 1973. Interactions between temperature and pore-fluid pressure during earthquake faulting and a mechanism for partial or total stress relief. Nature 243, 66–68.

Sibson, R.H., 1975. Generation of pseudotachylyte by ancient seismic faulting. Geophysical Journal of the Royal Astronomical Society 43 (3), 775–794.

Sibson, R.H., 1986. Earthquakes and rock deformation in crustal fault rocks. Annual Reviews of Earth Planetary Sciences 14, 149–175.

Sölva, H., Grasemann, B., Thöni, M., Thiede, R., Habler, G., 2005. Normal faulting associated with cretaceous SE-directed extrusion in the Eastern Alps (Italy/Austria). Tectonophysics 401, 143–166.

Spray, J.G., 1992. A physical basis for the frictional melting of some rock-forming minerals. Tectonophysics 204, 205–221.

Spray, J.G., 1993. Viscosity determinations of some frictionally generated silicate melts: implications for fault zone rheology at high strain rates. Journal of Geophysical Research 98, 8053–8068.

Swanson, M.T., 1992. Fault structure, wear mechanisms and rupture processes in pseudotachylytes generation. Tectonophysics 204, 223–242.

Trepmann, C.A., Stöckhert, B., 2003. Quartz microstructures developed during non-steady state plastic flow at rapidly decaying stress and strain rates. Journal of Structural Geology 25, 2035–2051.

Trepmann, C.A., Stöckhert, B., Dorner, D., Haamidzadeh, R., Küster, M., Röller, K., 2007. Simulating coseismic deformation of quartz in the middle crust and fabric evolution during postseismic stress relaxation — an experimental study. Tectonophysics 442, 83–104.

Warr, L.N., van der Pluijm, B.A., 2005. Crystal fractionation in the friction melts of seismic faults (Alpine Fault, New Zealand). Tectonophysics 402, 111–124.

White, S.R., 2001. Textural and microstructural evidence for semi-brittle flow in natural fault rocks with varied mica content. International Journal of Earth Sciences 90, 14–27.